Evaluating the use of high-frequency radar coastal currents to correct satellite altimetry

C. J. Roesler,[1] W. J. Emery,[1] and S. Y. Kim[2]

[1] Coastal altimeter waveforms may differ from the ones in the open ocean, either from rapid changes in the sea state or the presence of land within the satellite altimeter footprint. The optimal retracking method for an individual track may turn out to be a combination of several retrackers and may depend on the sea state. The coastal high-frequency radar (HFR) ocean surface currents, hourly interpolated with a resolution up to 2 km and an offshore range up to 150 km, are evaluated to validate the altimeter sea surface height (SSH) measurements. A method to derive HFR SSH mapped, with a varying spatial-scale optimal interpolation, from the HFR velocities has been implemented. Evaluated mainly in the regions farther than 25 km off the U.S. West Coast, the HFR SSH shows good agreement with Jason-1–2 altimetry products over the years 2008 and 2009. Three Jason-2 PISTACH retrackers and one generic open ocean retracker have been analyzed using the traditional 1 Hz sampling rate. Nearshore, an experimental reprocessing of the 20 Hz range measurements is also tested to check for a gain in along-track spatial resolution. Referencing to the HFR SSH indicate the need to have several retrackers available, even over the continental shelf, with Ice3 fitting better during Bloom events and MLE-4 (or Red3) for high sea states. These studies demonstrate the value of HFR as a potential tool to correct coastal altimeter SSH, refine their spatial resolution and provide some insight into the altimeter behavior as a function of ocean conditions.

1. Introduction

[2] The ocean plays an important role in shaping global climate on a rapidly changing planet. There is a need to observe, understand and model its diverse mechanisms. With more than 20 years of experience, satellite altimetry is a mature technology over the open ocean. With the adequate constellation of satellites, multimission altimetry provides globally homogeneous, high resolution, and regular mapping of mesoscale sea level and ocean circulation variations [*Morrow and Le Traon*, 2006]. Yet, altimetry and its application still face many challenges in coastal regions. These shelf regions, with intense human interactions, have a special role from an economical and environmental as well as recreational and safety perspectives. With the increase of anthropogenic global climate change, this zone is susceptible to greater environmental stresses and natural hazards.

[3] The accuracy of the nadir-looking, pulse-limited satellite radar altimeter sea surface height (SSH) measurement degrades in coastal region. The geophysical (tides, dynamic atmospheric correction) and environmental (ionospheric, dry and wet tropospheric, sea state corrections) corrections, that need to be applied to the altimeter range, become less reliable and yet more variable [*Andersen and Scharroo*, 2011] Second, the altimeter waveform (return echo) becomes distorted. Coastal waters differ from the open ocean due to rapid changes in bathymetry on the continental slopes, shallow waters, and the presence of coastline boundaries. This induces greater variability resulting in shorter time- and space scales. Possible rapid changes in sea state and/or the presence of land within the altimeter footprint affect the shape of the waveform. *Deng et al.* [2002, 2003] observed that the waveforms from ERS-2 and TOPEX/Poseidon could be affected by land up to 20 km off the Australian coast. Furthermore, waveforms can be degraded by the presence of unrealistic high-radar return cross sections (Sig0) in the altimeter footprint, called "Sig0-bloom events" [*Mitchum et al.*, 2004; *Tournadre et al.*, 2006]. These Sig0-bloom events can occur from weak wind patches as well as surface slicks, which create a highly reflective specular surface. These "contaminated" waveforms will not conform to the shape of the standard

[1] Colorado Center for Astrodynamics Research, Aerospace Engineering Sciences Department, University of Colorado, Boulder, Colorado, USA.
[2] Division of Ocean Systems Engineering, School of Mechanical, Aerospace and Systems Engineering, Korea Advanced Institute of Science and Technology, Yuseong-gu Daejeon, Republic of Korea.

Corresponding author: C. J. Roesler, Colorado Center for Astrodynamics Research, Aerospace Engineering Sciences Department, University of Colorado, Boulder, CO 80309, USA (carolyn.roesler@colorado.edu)

open-ocean Brown model formulated by *Brown* [1977]. The ocean geophysical parameter (SSH, significant wave height (SWH) and Sig0 related to surface wind speed) retrievals from these waveforms (retracking), fitted to the Brown model, will be unreliable.

[4] Recovering these coastal altimetry data would be valuable for studies of the complex coastal circulation, sea level change, and the impact on this coastal circulation. Some of the reasons are that the long-term altimetric measurements are repeatable, stable, and are the only long-term coastal measurements available in some remote areas. At present, altimetry alone, even with corrected high-resolution along-track coastal data, will not resolve all the various time- and spatial scales of coastal dynamics. The revisit time (10 days for Jason-2; a cycle) and the distances between tracks (∼100 km at 40° latitude for Jason-2) are too large, even with multiple altimeters. It must be considered as an important input to a coastal observing system. As such studies combining coastal altimetry and in situ data are adopted [*Ruiz et al.*, 2009; *Le Hénaff et al.*, 2010].

[5] Current altimetry products use generic open ocean processing that are retracked with the ocean Brown model and have been optimized for high-precision open-ocean variability along-track 1 Hz (or ∼7 km ground resolution) SSH. There is a loss of data in coastal regions from stringent quality checks (distorted waveforms, nonavailable corrections, etc.) [*Lee et al.*, 2009]. The use of altimeter data in the coastal zone requires the development of new retrackers, applying improved local corrections and reprocessing techniques to increase data coverage [*Cipollini et al.*, 2008; *Bouffard et al.*, 2008].

[6] These strategies have recently been implemented and demonstrated their values [*Birol et al.*, 2010; *Herbert et al.*, 2011]. The Coastal Altimetry (COASTALT) project provides experimental coastal data for several regions in the European seas (http://www.coastalt.eu). The Prototype Innovant de Système de Traitement pour l'Atimétrie Côtière et l'Hydrologie (PISTACH) coastal product [*AVISO/Altimetry*, 2010] is dedicated to the processing of Jason-2 altimeter data for the global coastal zone. But there are still many challenges to overcome for the full exploitation of coastal altimetry and their validation. Developing tools for the generation and quality check of these coastal products is a pertinent area of research. About 20 years of archived altimeter data in the coastal zones are waiting to be reprocessed.

[7] Improving the quality of altimeter geophysical retrievals is an important issue before using them for oceanographic applications. In this study, we will focus on the effect of retracking. Retracking is a key element to extend the use of coastal altimetry (whether pulse-limited or the new Cryosat-2 SAR/InSAR technology) and produces improved results in shallow-water tide modeling and sea surface topography determination [*Hwang and Chen*, 2000; *Deng and Featherstone*, 2006].

[8] Over the last few years, we have seen the development of new retrackers specific to coastal problems. Each has its own advantages and drawbacks. A review of waveform retracking methods can be found in *Gommenginger et al.* [2011]. To optimize the choice of the retracking method waveform, classifications are done [*Deng and Featherstone*, 2006] and are even included as a data element (waveform class) in the PISTASCH coastal product. However, there is a lack of a clear recommendation on which retracker to use depending on the situation. There is also a need to minimize the discontinuity of geophysical parameters from the open ocean to the coast. Changing retrackers from point to point along the track, depending only on the classification of the waveform, will create discontinuities from the relative biases between the various techniques. Consistency between the retrackers has to be investigated [*Deng*, 2004].

[9] The performance of retrackers can be estimated in a variety of ways. One possibility computes the statistics of residuals, using the geoid heights as a quasi-independent reference [*Deng and Featherstone*, 2006; *Hwang et al.*, 2006]. But the geoid may not be well resolved in the coastal regions. The validation of coastal altimetry data has been performed using tide gauges [*Lebedev et al.*, 2011] for the SSH, moored acoustic Doppler current profilers for near surface geostrophic velocity, and wave-rider buoys [*Gómez-Enri et al.*, 2011] for the SWH measurements. The problem is that in these validations one compares sparse point measurements that may not lie exactly over the satellite track in a highly dynamic region. High-frequency radar (HFR) radial velocities perpendicular to the satellite track were used to estimate the quality of altimeter-derived velocity. The geometry of the HFR configuration, however, limits the number of collocations [*Liu et al.*, 2012].

[10] This paper presents a novel approach to independently validate the coastal retrackers, using the HFR sea surface information that extends up to 150 km offshore along a continuous altimeter track and at the time of passage of the altimeter. The optimal method for altimetry retracking may turn out to be a combination of different retrackers for different parts of an altimeter track [*Deng and Featherstone*, 2006] or it may change for different cycles on the same track. The HFR data will ensure a continuity of the corrected altimetric SSH from the open ocean to the coast. These relationships will be explored in the west coast of the United States over the years 2008 and 2009, where the coverage of HFR surface current is excellent, with resolutions of 2 and 6 km depending on HFR-operating frequency. We will concentrate on Jason-1 and 2 data in this region (Figure 1) and on four retrackers, one conventional open-ocean retracker as well as three specific PISTACH retrackers. These four retrackers are available in the PISTACH data product and will hereafter be referred to as PISTACH retrackers for simplicity.

[11] Previous studies have compared altimetry and HFR surface current maps that support the potential of our methodology. *Saraceno et al.* [2008] show good correlations between a yearly time series of HFR velocities and an improved coastal SSH product at three locations along the Oregon coast. Two studies confirm that HFR contain more submesocale information [*Chavanne and Klein*, 2010; *Kim et al.*, 2011] than present-day satellite altimetry. Consequently, the 2 km HFR data can help assess the feasibility of creating a higher-resolution coastal product by exploiting the higher frequency 20 Hz (or ∼330 m ground resolution) altimetric range rate measurements and implementing new editing and filtering techniques. This enhanced resolution coastal data set will better resolve the smaller scale of oceanographic processes in coastal zones.
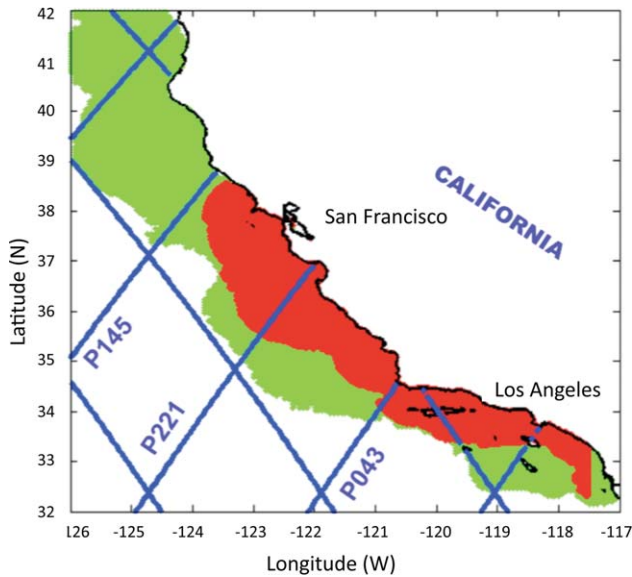
Figure 1. The U.S. West Coast HFR and altimeter data set coverage. Green corresponds to the HFR 6 km spatial resolution while the red is the 2 km resolution coverage. The blue lines are the ground tracks of the Jason-2 altimeter satellite.

[12] As part of the growing ocean observing infrastructure, HFR and altimeter data are complementary; through their respective instrument design, they observe different aspects of the coastal ocean. It is our goal, here, to fit HFR coastal currents to altimeter sea levels. The experience gained from a systematic comparison of both data sets, can provide hints on how to correct conventional coastal altimetry in regions where no HFR arrays are deployed and how to test the data quality of future altimetry missions, better suited for coastal observations.

[13] In this first study, which provides the basis for further in-depth investigations, the region of interest will be mainly 25 km till about 150 km (which represents the furthest extent of the HFR data) offshore. Our domain does not include the nearshore area, except briefly in section 4.2.2. This was chosen to reduce the errors in range correction that accumulate in the SSH altimetric estimates. Probably, a more specific HFR processing would be required in the nearshore region that includes costal boundaries. The potential of HFR to correct coastal altimetric heights can still be explored, because there are unresolved issues in retrieving altimetry range in this domain as aforementioned. For example, *Lee et al*. [2010] find that, on average for Jason-2 from July 2008 to July 2009, a retracker developed for nonocean surfaces improves the Brown-retracked SSH over the Californian continental shelf.

[14] The following questions will be addressed. How should we process the HFR surface current data to make them comparable with altimeter sea level measurements? How well are they related and what are the limitations of this comparison? Is there any information gained by validating the 2 km HFR data and high-frequency altimeter data? Can we use HFR to detect invalid segments of the traditional open-ocean retracked altimeter measurements and, if so, to decide which PISTACH retracker better fits

the segment as well as evaluate the performance of the retrackers under various sea-state conditions?

[15] This paper will be organized as follows; section 2 presents the satellite altimetry and HFR data. In section 3, the methodology used to derive sea level measurements from HFR is explained. In section 4, the HFR SSHs are compared with altimetric SSH for three differently processed altimeter data sets as well as for several PISTACH retrackers. Examples of issues arising from several sea states are also examined. A discussion of the results, their limitations, and possible future extensions conclude the article in section 5.

2. Basic Principles and Data

2.1. Altimetry

2.1.1. Altimeter Data Sets

[16] We use three different altimeter data sets all distributed by AVISO. The first one is the weekly multimission altimetry merged sea level anomaly (MSLA) product [*AVISO/Altimetry*, 2013], gridded SSHs computed with respect to a 7 year mean, on a $1/3° \times 1/3°$ Mercator grid. This product combines data from different missions. More specifically, we use the delayed-time, updated series. This data set usually has no values for offshore distances closer than about 20 km, where the data has been flagged "bad" due to its proximity to land. We picked the weekly 2008 time series for the Californian coast in the region where we have coincident HFR currents.

[17] The second set is the global delayed-time along-track sea level anomalies (SLA) product [*AVISO/Altimetry*, 2012], which provides standard open-ocean 1 Hz (ground track spacing of 6 km) along-track sea level anomalies computed with respect to a 7 year mean, with all standard corrections already applied. The time series is for the year 2008 for Jason-1, corresponding to cycles C220–C256 for the satellite-track P221, which terminates in Monterey Bay, California (Figure 1). Note that the number of this pass was for Jason-1 prior to its shift to the interleaved ground track in February 2009 and now corresponds to the Jason-2 pass denomination. Jason-type satellites have a 10 day repeat cycle.

[18] For the previous two sets, the corrections applied to the SSHs are from the regular open ocean processing; no specific coastal corrections have been applied.

[19] The third set is the Jason-2 PISTACH coastal product [*AVISO/Altimetry*, 2010]. For each correction affected by the proximity of land (such as the wet tropospheric correction), it offers a varied choice of correction scenarios. PISTACH also gives output for three new retracking schemes at the 20 Hz rate: Oce3, Red3, and Ice3. These three specific PISTACH retrackers will be analyzed together with one of the conventional Jason-2 deep-ocean retracker MLE-4. The latter is available in the PISTACH database and corresponds to the MLE-4 provided in the Sensor Geophysical Data Record (SGDR version "T" and the new SGDR version "D" (as of August 2012) [*OSTM*, 2011]).

[20] The Oce3 retracker represents the output of MLE-3 performed on a denoised waveform, filtered after a singular value decomposition (SVD) [*Severini*, 2010]. The Red3 retracker also uses MLE-3 but is done on a restricted

analysis window around the leading edge, to remove the eventual gates corrupted by the effects of land. The Ice3 retracker is a 30% threshold method [*Davis*, 1997], also implemented on a restricted analysis window.

[21] The PISTACH sea-level anomalies will be computed from the 20 Hz data stream for the various retrackers. For the specific coastal corrections we chose: the global ionospheric map (GIM) correction, the decontaminated water vapor correction where the microwave radiometer (MR) brightness temperatures are decontaminated from land before applying the water vapor retrieval algorithm [*Desporte et al.*, 2007] and the tides from the FES2004 solution [*Lyard et al.*, 2006]. The MLE-4 derived sea state bias (SSB) is applied to each retracker's range, because it is the only SSB field given in the PISATCH product. This assumption may not hold as each retracker behaves differently as a function the sea state. The 20 Hz SSB is linearly interpolated from 1 Hz measurements. The mean sea surface (MSS) from the Danish Space Center MSS DNSC08 is used, but this is not so critical, because we remove a mean of the time series for our final sea-level heights product. All other corrections are the standard ones. The waveforms are extracted from the corresponding SGDR product.

[22] For the PISTACH sets, the time series along P221 is analyzed from August 2008 until the end of December 2009, corresponding to cycles C004–C054 (two cycles C005 and C018 are not included). The PISTACH data will be processed in two different manners as described in section 4.2.

2.1.2. Altimeter Waveforms

[23] Conventional satellite altimeters are nadir-pointing instruments that emit short pulses reflected by the sea surface. The geometry of the footprint is pulse limited, and pulse compression is used to achieve high-accuracy ranging. The time evolution of the echo, the waveform, represents the mean return backscattered power as a function of time. To reduce speckle, the individual return echoes are averaged onboard, typically over 100 successive echoes (at Ku-band) over a period of 50 ms. These 20 Hz waveforms are transmitted to the ground, where retracking (ground retracking) is applied to refine the extraction of the oceanic parameters. For open-ocean generic products, the data are averaged to 1 Hz [*Chelton et al.*, 2001].

[24] Over water, after the pulse hits the surface, the illuminated surface area grows from a point to a disk and then spreads as an annulus increasing in diameter but with a constant surface area. The corresponding waveform shows a characteristic shape with a sharp rise to a maximum level (leading edge) followed by a gradually sloping trailing edge, as the off-nadir signal slowly reaches the edge of the radar beam. The waveform provides the range between the satellite and the surface at nadir via the two-way travel time of the transmitted pulse, the SWH via the slope of the leading edge and the backscattering coefficient Sig0, which represents the surface roughness via the returned power (Figure 2). This ocean shape can be represented by an analytical *Brown* [1977] model. For the Jason-1 and Jason-2 altimeters, considered in this study, the waveforms of 104 samples (or range gates) are retracked using a maximum likelihood estimator (MLE) fit to the Brown model. The MLE-3 retrieves three geophysical parameters (range,
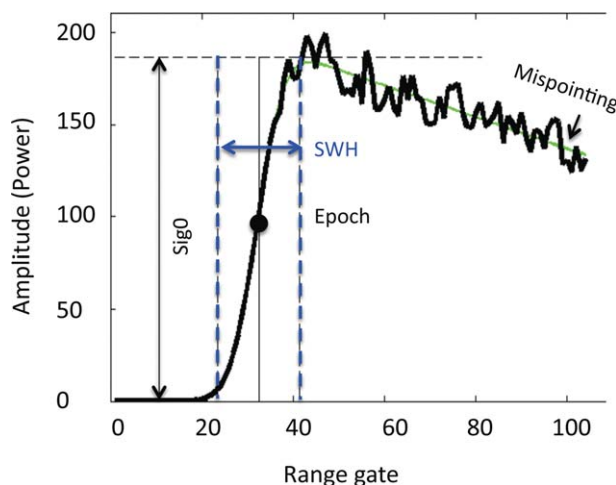

Figure 2. Jason-2 Ku Band Echo (in black). Brown waveform (in green) and parameters retrieved by MLE-4.

SWH, and Sig0); the MLE-4 also estimates the antenna-mispointing angle (slope of the trailing edge).

[25] The Brown model has been derived from the physical properties of a rough and homogeneous scattering surface for near-normal incidence. Although, different refined analytical forms exist, one of the main assumptions related to the surface properties (not the instrument, or pulse shape) are that the sea surface is homogeneous over the footprint and that the probability distribution function of the surface slope and elevation has a predefined shape, essentially Gaussian. When this is not the case, the waveform will not conform to the Brown model, and new retracking strategies will need to be implemented.

[26] The altimeter waveforms may be corrupted by non-uniform radar return Sig0 in the altimeter footprint. In the case of Sig0-blooms, there are occurrences of unusually high Sig0 due to highly reflecting ocean patches. The presence of these higher Sig0 values may signal a breakdown in the typical Brown open ocean waveform model (Figure 3). First of all, the onboard tracker normally centers the waveform leading edge at a predefined gate range (32.5 for Jason-2) to keep the waveform well centered in the analysis window. But with distorted waveforms the leading edge can shift. This can be observed in the consecutive 20 Hz waveform series of Figure 3a, in the presence of a Sig0-bloom around 30 km off the coast, for cycle 26 on P221 (as well as nearshore, for waveforms contaminated by land). Second, Sig0-blooms can create various waveform shapes. The distortion is not predetermined (Figures 3c and 3d): the trailing edge slope could be increasing or decreasing; the peakiness increased; there could be the presence of a V-shape or round pattern similar to the ones observed during rain events [*Quartly et al.*, 1998].

[27] The waveforms affected by land will not be included in this study. The interested reader can refer to *Gommenginger et al.* [2011]. For completion, we will mention that for an ocean to land transition, the altimeter footprint will gradually contain more and more land returns. More waveform samples will progressively be perturbed starting from the trailing edge and moving toward the leading edge. The shape of the coastline, the relief, and the
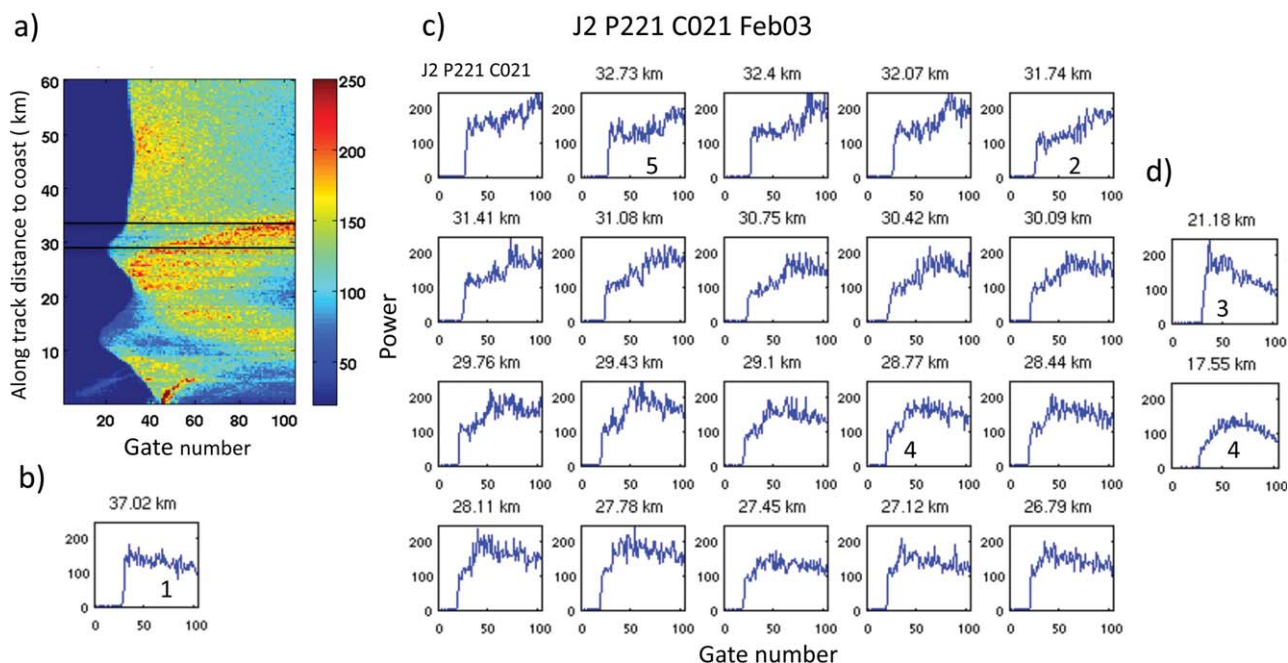
Figure 3. (a) The 20 Hz waveforms from Jason-2 Cycle 26 pass 221, 3 February 2008; (b) typical Brown waveform; (c) consecutive 20 Hz waveforms, 30 km off shore in the presence of a Sig0-bloom event, over the region indicated by a black box in Figure 3a. (d) Other "bloom" waveform shapes at 21.18 and 17.55 km. (1) Brown waveform, (2) increasing trailing edge, (3) peakiness increased, (4) round pattern, (5) V-shape.

backscattering properties of the terrain will produce a variety of coastal waveform shapes.

[28] Furthermore, over the shelf regions, the ocean characteristics are expected to change and have smaller spatial scales. There could be a variety of waveforms affected in a yet not well-defined way, because the dynamics of the system are still not well understood.

2.1.3. Altimetric Sea-Level Height Corrections

[29] Retracking improves the estimate of the range, but it still needs to be adjusted for atmospheric path delays (dry/wet and ionospheric) as well as for an electromagnetic bias SSB. These can be problematic in the littoral regions. The Jason altimeters carry onboard MRs to correct for the water vapor but close to shore the MR footprint will be contaminated by land. Due to technical improvements the advance microwave radiometer (AMR), onboard Jason-2, water vapor estimates are probably not corrupted by land until ~25 km offshore relative to 50 km for the Jason-1 MR. For the highly variable in time and space water vapor corrections, different strategies exist, such as correcting the altimeter radiometer due to land contamination [*Desporte et al.*, 2007; *Brown*, 2010]. The frequency-dependent ionospheric path delay is calculated from the dual-frequency altimeter (C-band and Ku-band); but land also contaminates their footprints (C-band has a larger beam width). The ionospheric correction GIM derived from the global positioning system (GPS) network is recommended in coastal areas.

[30] The SSB correction compensates for the bias of the altimeter range measurement toward the troughs of the ocean waves, as well as for an instrumental bias. It depends on the sea state (wave types and wind field). The open ocean SSB is empirically determined from the SWH and the wind speed [*Tran et al.*, 2006]. In the coastal zone, with complex wind and wave dynamics, this empirical relationship may not be valid. However, we have opted to include it.

[31] Finally, once the range has been corrected, the SLA is computed relative to a MSS level:

$$\text{SLA} = \text{Satellite height} - \text{Corrected range} - \text{MSS} - \text{Tides height} - \text{Atmospheric pressure loading,}$$

where Corrected range = Altimeter Range
+ Atmospheric corrections + SSB.

[32] Other important considerations in the coastal regions are the tidal and high-frequency atmospheric pressure loading corrections that are less accurate. All of the environmental aforementioned corrections are subjects of ongoing research.

[33] Depending on the altimeter data set used and the focus of the analysis (more on the open ocean or on the littoral regions), some improved corrections will, or will not, be implemented. It is important to acknowledge these problems so that we understand that the altimeter segments could be affected by these corrections and, each one of them, in variable amounts and at variable distances from the shoreline.

2.2. High-Frequency Radar

[34] Operational shore-based HFR systems provide hourly surface current maps averaged within the upper meter depth, with an offshore range of 50–150 km and a spatial resolution of 0.5–6 km, depending on the radar operating frequency [*Barrick et al.*, 1977; *Lipa and*
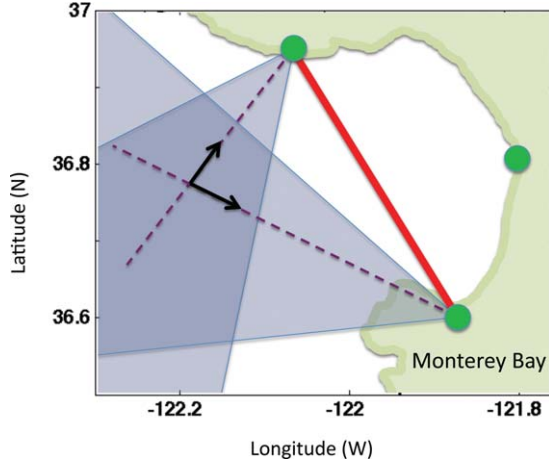
Figure 4. HFR geometry in Monterey Bay. Green dot: HFR radar sites. Red line: Baseline between two stations. Blue zone: part of HFR coverage area. Dotted line: radial line. Vector: radial surface current.

Barrick, 1986; *Ohlmann et al.*, 2007]. The HFR emits a high-frequency radio signal in the range of 5–25 MHz, which are backscattered from the ocean surface. The ocean gravity waves with a wavelength of half the transmitted wavelength (Bragg scatter) will reflect back coherently and result in a strong peak in the retuned energy spectrum. The Doppler shift of the peak indicates movement of these gravity waves in a direction either toward or away from the HFR site (radial). The ocean gravity waves have a known phase velocity and ride on the surface current. Subtraction of the theoretical phase velocity gives the radial ocean surface current velocity [*Paduan et al.*, 1997].

[35] Individual HFR reports the surface radial velocity map, which is a set of projected velocity components of the true current field with respect to the radar-bearing angles. Thus, in order to extract a vector current map, multiple radial velocity maps are required (Figure 4). The geometry of the HFR sites defines the coverage where the current estimates are reliable. For instance, the baseline is a straight line between two radars [*Paduan et al.*, 1997]. Along the baseline, the current estimate can be limited as the radial velocities from the two sites are nearly parallel. However, the postprocessing of the HFR radials can eliminate most of the artifacts along the baseline [*Kim et al.*, 2008, 2011].

[36] The uncertainty in the HFR-derived surface current measurements can be influenced by several factors such as antenna beam pattern, signal-to-noise ratio (SNR), sea state related to wind speed and direction, radar geometry, and interference of radar frequency. For example, the locally calibrated radar beam pattern can improve the quality of radial maps and help to produce the realistic current field [*Paduan et al.*, 2006]. Moreover, the low SNR of Bragg scatter echo due to weak wind condition can hinder to estimate radial solutions accurately. The baseline due to radar geometry can be placed on land or in the sea, which may generate spurious vector solutions in the near-coast regions. The uncertainty estimated from both independent observations and HFR radial velocity measurement itself ranges from 3 to 12 cm/s (see *Laws and Paduan* [2011] and *Kim et al.* [2011] for more details).

[37] In this paper, we analyze the optimally interpolated HFR-derived surface currents off California coast for 2 years (2008–2009) with the resolution of 2 and 6 km in space and hourly in time [*Kim et al.*, 2008; *Kim*, 2010]. The 2 km (6 km) resolution HFR data have a minimum nearshore range of 3 km (9 km) and maximum offshore range of 50 km (150 km) (Figure 1).

3. Analysis Method: Retrieval of Synthetic SSH From HFR Currents

[38] Altimetry maps the vertically integrated SSH that can be related to the geostrophic flow, whereas HFR data gives us a surface total velocity and includes ageostrophic processes that need to be removed to compare the two data sets. In this study, an optimal interpolation (OI) was chosen to retrieve the geostrophic currents from the total velocity surface measured by the HFRs. More precisely, the OI estimates the nondivergent stream function and, assuming near-geostrophy for the associated nondivergent current field, the HFR two-dimensional SSH field. The OI requires an analysis of the time- and spatial scales of the coastal oceanic features. These features are expected to vary with the distance to the coastline and/or with the bathymetry and thus may vary regionally.

3.1. Optimal Interpolation

[39] The variable to be estimated is the stream function ψ, because we are interested in capturing the geostrophic (nondivergent) part of the HFR-observed flow. If the flow is assumed to be nearly geostrophic, there is a linear relationship between the stream function and the observed velocities: ($u = -\mathrm{d}\psi/\mathrm{d}y$ and $v = \mathrm{d}\psi/\mathrm{d}x$). The stream function ψ can, then, be calculated directly from the HFR-derived currents using an OI [*Bretherton et al.*, 1976; *Wilkin et al.*, 2002].

[40] The velocity observations are concatenated in the data vector $\phi^{\mathrm{obs}} = [\mathbf{u}\ \mathbf{v}]^{\mathrm{T}}$ (T denotes the vector transpose), where $\mathbf{u}$ and $\mathbf{v}$ refer to the suite of measurements (u_i) and (v_i) done at distinct locations with velocity components $[u_i\ v_i]^{\mathrm{T}}$. The observations are inexact, $\phi_i^{\mathrm{obs}} = \phi_i + e_i$, where ϕ_i is the true value and e_i is the measurement error, assumed to be uncorrelated with each other. The vector stream function estimate at the OI grid point locations is given by

$$\psi^{\mathrm{est}} = C_{\mathrm{md}}\,(C_{\mathrm{dd}})^{-1}\,\phi^{\mathrm{obs}} \tag{1}$$

where C_{md} is the covariance of the estimated model with the data:

$$(C_{\mathrm{md}})_{\mathrm{ki}} = \langle \psi_k^{\mathrm{est}}\,\phi_i^{\mathrm{obs}} \rangle = \langle y_k^{\mathrm{est}}\,\phi_i \rangle \tag{2}$$
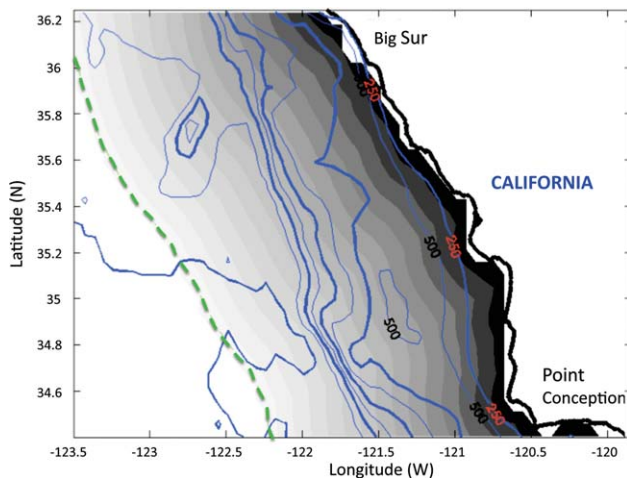
[41] ($\langle\ \rangle$ is the expected value) C_{dd} is the covariance of the data with each other:

$$(C_{\mathrm{dd}})_{ij} = \langle \phi_i^{\mathrm{obs}}\,\phi_j^{\mathrm{obs}} \rangle = \langle \phi_i\phi_j \rangle + \langle e_i e_j \rangle = \langle \phi_i\phi_j \rangle + e^2\delta_{ij} \tag{3}$$

where e^2 is the noise-error variance of the surface currents.

[42] The uncertainty covariance matrix of the estimate is defined as

Figure 5. Data set geography between Big Sur and point conception. Gray scale: 10 km distance-band regions from 150 km to the coast. Blue contours: bathymetry with an interval of 500 m from 500 to 4000 m; bold lines every 1000 m from 1000 to 4000 m; light lines every 1000 m from 500 to 3500 m. Dotted green line: boundary of HFR 6 km resolution.

$$\xi = s_\psi^{2.}I - (C_{\mathrm{md}})(C_{\mathrm{dd}})^{-1}(C_{\mathrm{md}})^t \qquad (4)$$

where s_ψ^2 is the variance of ψ and I is an identity matrix.

[43] At this preliminary stage, we will assume that the low-frequency parts of the velocity components are nearly geostrophic [*Tisch et al.*, 1989; *Chereskin and Trunnell*, 1996] The hourly HFR velocities contain HF components arising from tides and short-term wind events that need to be removed in order to better approximate the observed underlying geostrophic flow. This will de done through temporal averaging. The study of the velocity temporal scales over the coastal transition zone will provide the information about how much temporal averaging can be done, while still preserving the local structure that is required to compare with the instantaneous altimeter measurements. Finally, we need to find a functional form of the various spatial covariance functions derived from the observed HFR velocity spatial scales and structures.

3.2. Data Covariance Scales

[44] The first analysis was done along the southern California coast between Big Sur and Point Conception, where the coastline is relatively straight (Figure 5). For this analysis, we are using a 3 day running average of a 2008 time series sampled every 3 days, from hourly HFR measured ocean surface currents resampled and postprocessed to 6 km resolution. Three-day composites have been selected to remove the tidal and inertial current components in these currents. To depict how the time- and space scales vary with the distance to coast, the HFR velocity covariances have been analyzed for fifteen 10 km distance-band regions from 150 km offshore to the coast (Figure 5). The velocities have been projected on to across-shelf velocities, u; and alongshelf velocities, v; corresponding to the across-shelf axis X, and alongshelf axis Y, respectively. A 2008 seasonal mean has been removed from the data, corre-

sponding to the two characteristic current patterns of the California coastal current system.

[45] The HFR temporal covariances were analyzed over each 10 km wide region and averaged over the year 2008. A decrease of the *e*-folding timescale from about 10 days in the open ocean to 3 days closer to shore can be detected (Figure 6). Over the complete domain, the data will de relatively highly correlated over the lowest timescale, which is 3 days. Hence, as a first approximation of the observed geostrophic flow we will use a 3 day averaging of the HFR velocities. This may be less representative of conditions in the near-coastal region due to smoothing; but for this first exploration, which compares altimetry and HFR, mainly, on coastal regions further than 25 km offshore, this level of smoothing should still be adequate. This 3 day temporal averaging was also chosen in the deep ocean by *Bretherton et al.* [1976] and *Wilkin et al.* [2002]. We acknowledge that averaging over 1 or 2 days should also be tested in the future. For example, using HFR velocities, several authors average over 2 days to retrieve the low-frequency subinertial currents [*Chavanne and Klein*, 2010; *Saraceno et al.*, 2008].

[46] Also for submesoscale structures of the order of 10 km, the Rossby radius of deformation may be approaching 1 and the advective terms cannot be neglected. Nevertheless, even if the observations are divergent, the divergence in the data will be removed by applying this specific OI gridding algorithm, which enforces nondivergence. The validity of the assumption can then be assessed by comparing the observations and the derived gridded geostrophic currents.

[47] Next, the HFR velocity spatial covariances are estimated by computing the data spatial covariance values at zero time lag. The spatial covariances are binned according to spatial lags across-shelf X and alongshelf Y, normalized relative to the maximum, and averaged over the year of 2008 (Figure 7) for each 10 km wide band. The blank places in (Figure 7) represent areas of no data coverage; the coast is on the right, the open ocean is on the left. The features in Figure 7 make reasonable sense. The length scale of the across-shelf covariance (C_{uu}) grows in both directions (X and Y) with increasing distance offshore. This is consistent with the coastal boundary limiting eddy size and is the theoretical pattern for coastally trapped waves across-shelf velocity. We also observe, more or less, the same pattern in the alongshelf covariance (C_{vv}) especially in the central small spatial-lag area (central red area in Figure 7). Although, in contrast to C_{uu}, there is a component that stays elongated in the Y, alongshelf direction, visible in the slightly larger spatial-lag area (yellow area in Figure 7). Again, this is consistent with coastally trapped wave theory. The distance from the coast does not appreciably affect the alongshelf scale for the alongshelf velocity.

[48] For the purpose of this study, we will fit a theoretical spatial covariance function to the central (red) section and assume that C_{vv} grows in both directions with increasing distance offshore. By making this approximation and from the structures of both observed spatial covariances, we can then assume the velocities to be consistent with the statistics of a locally homogeneous, isotropic turbulence. This implies that the stream function spatial covariance $C_{\psi\psi}$ is related to the velocity spatial covariances
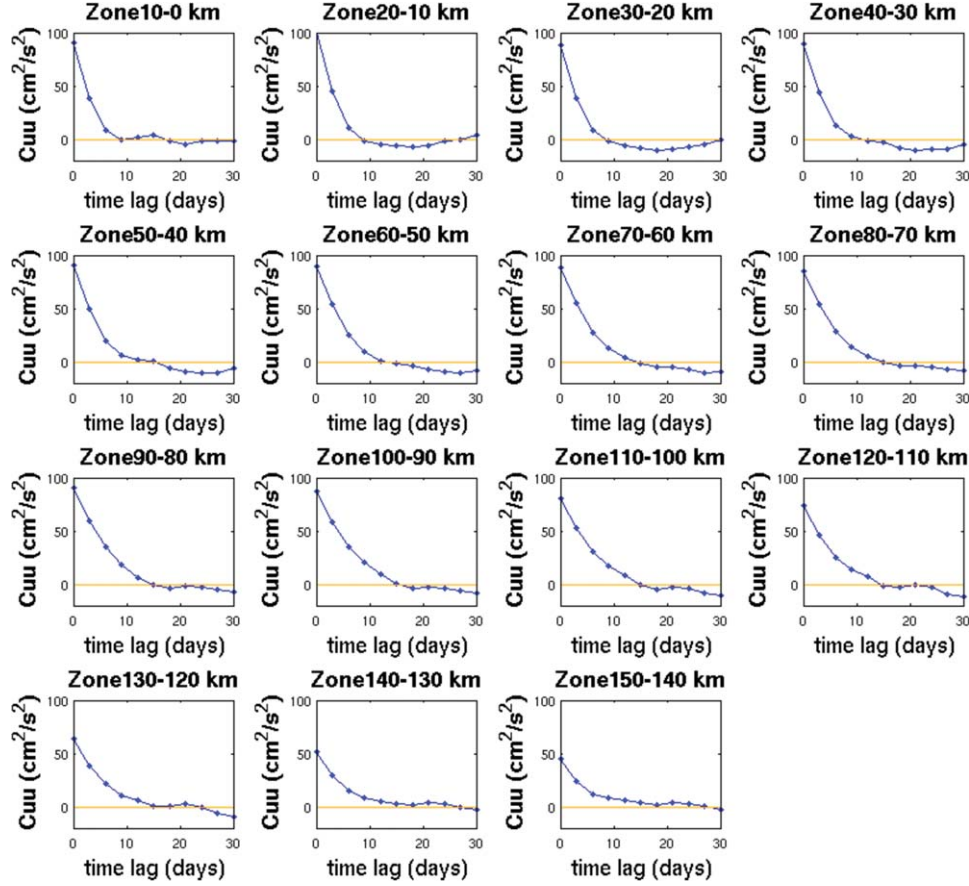
Figure 6. Temporal covariance of the across-shelf (*u*) HFR velocity data at zero spatial lag, averaged over the year 2008 for each 10 km width region. The offshore region increases from top to bottom and left to right.

[*Bretherton et al.*, 1976; *Wilkin et al.*, 2002]. We use the *Walstadt et al.* 1991] stream function ψ for the normalized spatial covariance defined as

$$C_{\psi\psi} = \left(1 - r^2/b^2\right)\exp\left(-r^2/a^2\right)$$

from which the theoretical velocities covariances can be derived [*Wilkin et al.*, 2002]

$$
\begin{aligned}
C_{uu} &= (X^2/r^2)(T-S) + S \\
C_{vv} &= (Y^2/r^2)(T-S) + S \quad \text{where} \quad T = -1/r(\partial C_{\psi\psi}/\partial r) \\
C_{uv} &= (XY/r^2)(T-S) \qquad\qquad\quad S = -1/r(\partial^2 C_{\psi\psi}/\partial^2 r) \\
C_{\psi v} &= YT \qquad\qquad\qquad\qquad\qquad\quad r = (X^2 + Y^2)^{1/2} \\
C_{\psi v} &= -XT
\end{aligned}
$$

(5)

[49] Figure 8 shows the good match between the observed and fitted covariances for the offshore region between 50 and 60 km, normalized and averaged over the year 2008. We fit the parameters *a* and *b* in equation (1) for each zone. We find, for example, in the offshore zone between 50 and 60 km, $a = 50$ km and $b = 70$ km and in the offshore zone between 20 and 30 km, $a = 35$ km and $b = 50$ km.

[50] In conclusion, we can directly estimate the stream function, proportional to the SSHs (assuming geostrophy),

from the observed HFR currents with an OI method that uses locally varying spatial scales depending on the distance of the OI grid point from the coast. The covariance matrices C_{md} and C_{dd} in equation 1 are:

$$C_{dd} = \begin{pmatrix} C_{uu} + e^2 I & C_{uv} \\ C_{uv} & C_{vv} + e^2 I \end{pmatrix} \quad \text{and} \quad C_{md} = \left(C_{\psi u}\, C_{\psi v} \right)$$

(6)

[51] In this OI implementation, we incorporated a linear change in spatial scale over the continental shelf. Thus, each point in the domain of interest is assigned a specific spatial scale depending on its distance from the coast. We selected observations in an area with a radius selected as the local spatial scale to reduce the amount of observations and the computational time.

[52] The velocity-noise error for the HFR is assumed to be constant $e = 15$ cm/s, although in reality, this error varies depending primarily on the radar and current geometry, less on weather conditions and in our case on how well the initial geostrophic assumption is satisfied. This value was chosen considering the typical errors found in the HFR velocities (section 2). From a total velocity error of 15 cm/ s, the individual error component could be lowered, and after a 3 day averaging, the errors could decrease even more, if the geostrophic component is properly captured.
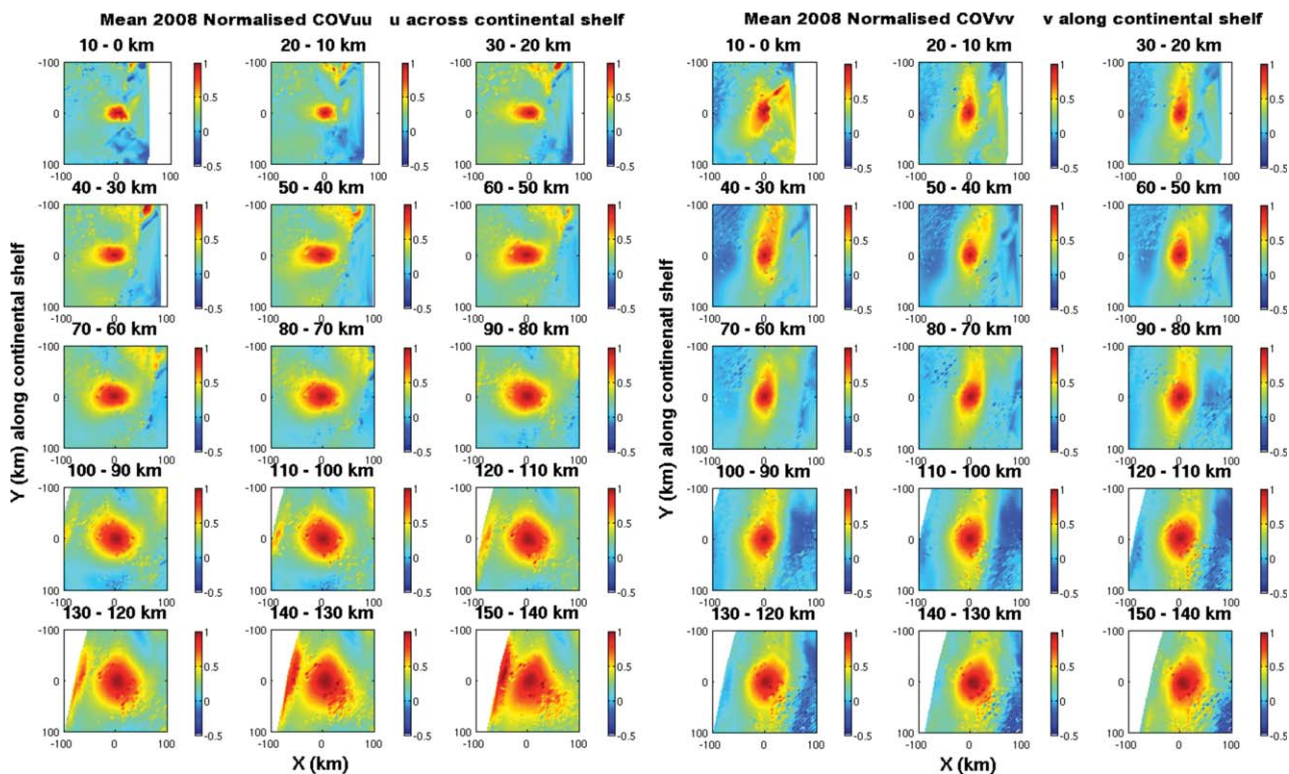
Figure 7. Covariances of HFR velocity (left) C_{uu} and (right) C_{vv} at zero time lag, for each 10 km wide region, binned according to spatial lag X (cross-shelf) and Y (alongshelf), normalized and averaged over 2008. The seasonal mean has been removed from the across-shelf velocity, u, and along-shelf velocity, v. The offshore region increases from top to bottom and left to right.

Furthermore, the residuals of the optimally interpolated field should be consistent with the assumed error variance of the data. Over 2008, we find that the root-mean-square (RMS) difference of the HFR and the OI-mapped velocities in the u and v components are 3.9 and 4.4 cm/s less than the estimated error variance of 15 cm/s. Also an RMS error of 10% in the HFR velocity observations results in an RMS error of about 4 cm/s in the OI-derived geostrophic velocities, which is, again, smaller than 15 cm/s (even if we take into account the factor of 2 (section 4)).

[53] We implemented this OI mapping method for the region of the Jason-1 track P221 that terminates in Monterey bay (Figure 9). The bathymetry found along this area of the California coast causes the formation of eddies [*Ikeda et al.*, 1984; *Hickey*, 1998; *Strub et al.*, 1991]. This is a region prone to having large sea level anomaly (SLA) variations and a good one to test our methodology. In Figure 10, we present the results of the OI from the 2 km resolution HFR velocities, for the along-track pass P221 on 6 September 2008. The mapped SSH has been computed using a varying spatial scale (Figure 10, right) versus using a single spatial scale, chosen to be the one for the zone between 50 and 60 km over the continental shelf (Figure 10, left). The varying spatial-scale method clearly shows more details in the dynamic height structure.

[54] The OI methodology was explained for the more complex case of a direct comparison of HFR observations with the instantaneous altimeter along track on an OI grid of 2 or 6 km resolution. But we will also adapt the method-

ology to compare HFR data with the weekly MSLA product (section 2.1.3) on a 1/3 ° × 1/3 ° grid. This is simpler. First, we can directly average the HRF currents over a week, the same time sampling. Second, the OI grid is chosen to be the same as the MSLA grid, thus about 30 km resolution. This resolution imposes a limit on the spatial-scales features that can be detected to more than 60 km. So, in this case, we will only use one spatial scale chosen to be the one for the zone 50–60 km.

[55] Note that the HFR synthetic SSHs contain an unknown bias due to the geostrophic relationship ($u = -g/f$ $\partial SSH/\partial y$ and $v = g/f \partial SSH/\partial x$), where f is the Coriolis parameter and g is the gravitational acceleration.

4. Results

[56] The HFR synthetic SSHs are compared with altimetric SSH for three differently processed altimeter data sets as well as for several PISTACH retrackers. Examples of issues arising from various sea states are also examined.

[57] In order to obtain consistent time series of HFR and altimeter SLA, i.e., relative to the same reference level, the mean of the sea level time series is removed from both SSH data sets. This mean is adjusted for each specific data set used. Also we notice that, in general, to match the variations of the altimeter SLA, the HFR sea levels need to be amplified by a factor of 2. We think this is due to the smoothing inherent in the OI methodology, but the exact reason for this discrepancy requires further investigation.
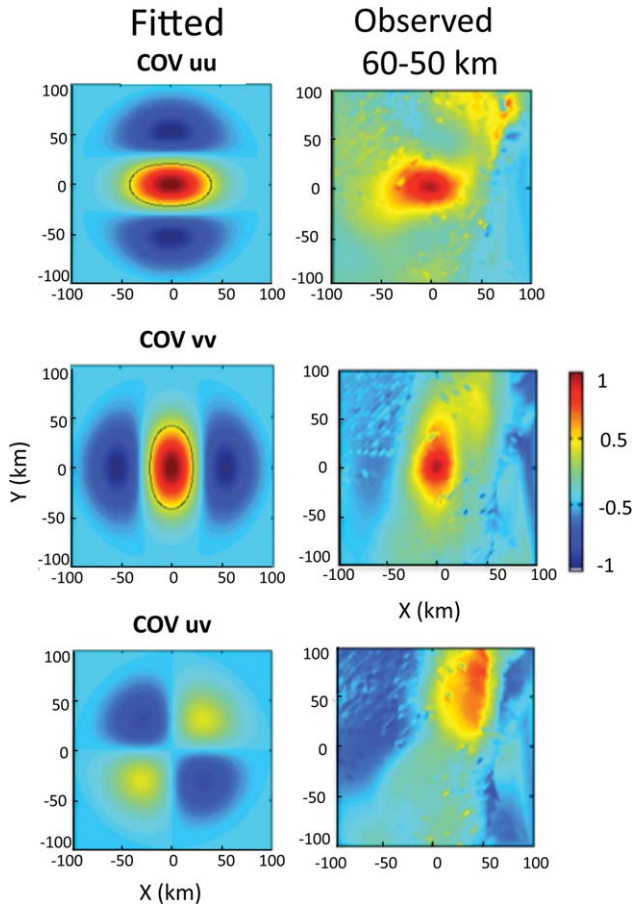
Figure 8. (right) Observed and (left) fitted covariance functions for the across-shelf (*u*) and alongshelf (*v*) HFR velocities in the 60–50 km offshore zone.

This estimated factor of 2 has been derived from the least squares method (refer to section 4.1.2 for details) and is applied to each HFR-inferred sea level set.

4.1. Comparison of HFR Over the Open Ocean With Standard Altimetry Product

[58] The comparison of HFR and altimeter SLA over the wide continental shelf, which we refer to as the open ocean
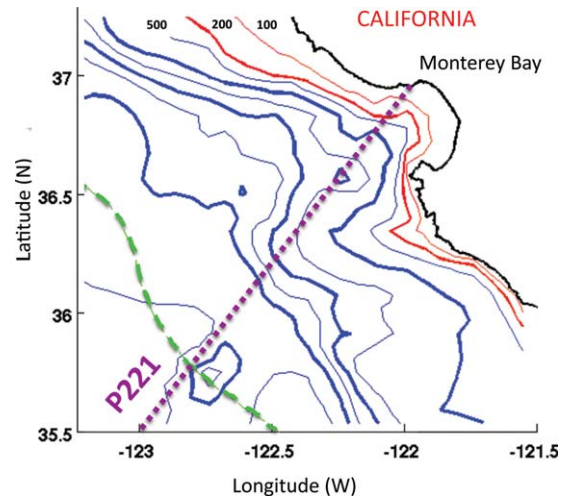
Figure 9. Monterey Bay bathymetry. Red lines: bathymetry, light 100 m, bold 250 m. Blue lines: bathymetry, bold every 1000 m from 1000 to 4000 m, light every 1000 m from 500 to 3500 m. HFR limit: long dotted line. Jason-2 P221: small dotted line.

(25–150 km offshore), will set the criteria for the feasibility of the method. This is an area where altimetry is assumed to be reliable.

4.1.1. HFR and MSLA

[59] First of all, we will analyze the weekly MSLA over the year 2008 with the corresponding weekly HFR synthetic SLAs, derived from the OI, on a $1/3° \times 1/3°$ grid for the Californian coastal region. The mean of the sea level time series is removed from both data sets. To adjust for the unknown bias for each weekly HFR sea levels (derived from the OI method), an estimate of the bias over the complete region is computed, and then subtracted. The bias for week w is computed by taking the mean of the difference between the HFR and MSLA sea levels, over the entire region.

[60] We created a movie for the weekly time series, of both sets presented as snap shots in Figure 11 with a sampling of every 6 weeks. After August 2008, the field
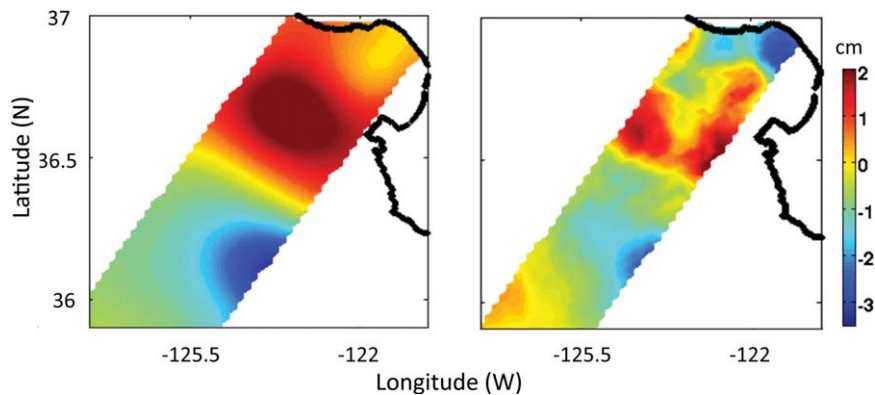
Figure 10. HFR synthetic SSH in centimeters, computed at the Jason-2 time on 6 September 2008 along-track P221. Effect of using a single spatial scale chosen at the (left) 50 km zone and the (right) varying spatial scale OI method, on a 2 km resolution grid. The computation time is faster for the single spatial-scale method, so the output area is slightly larger.
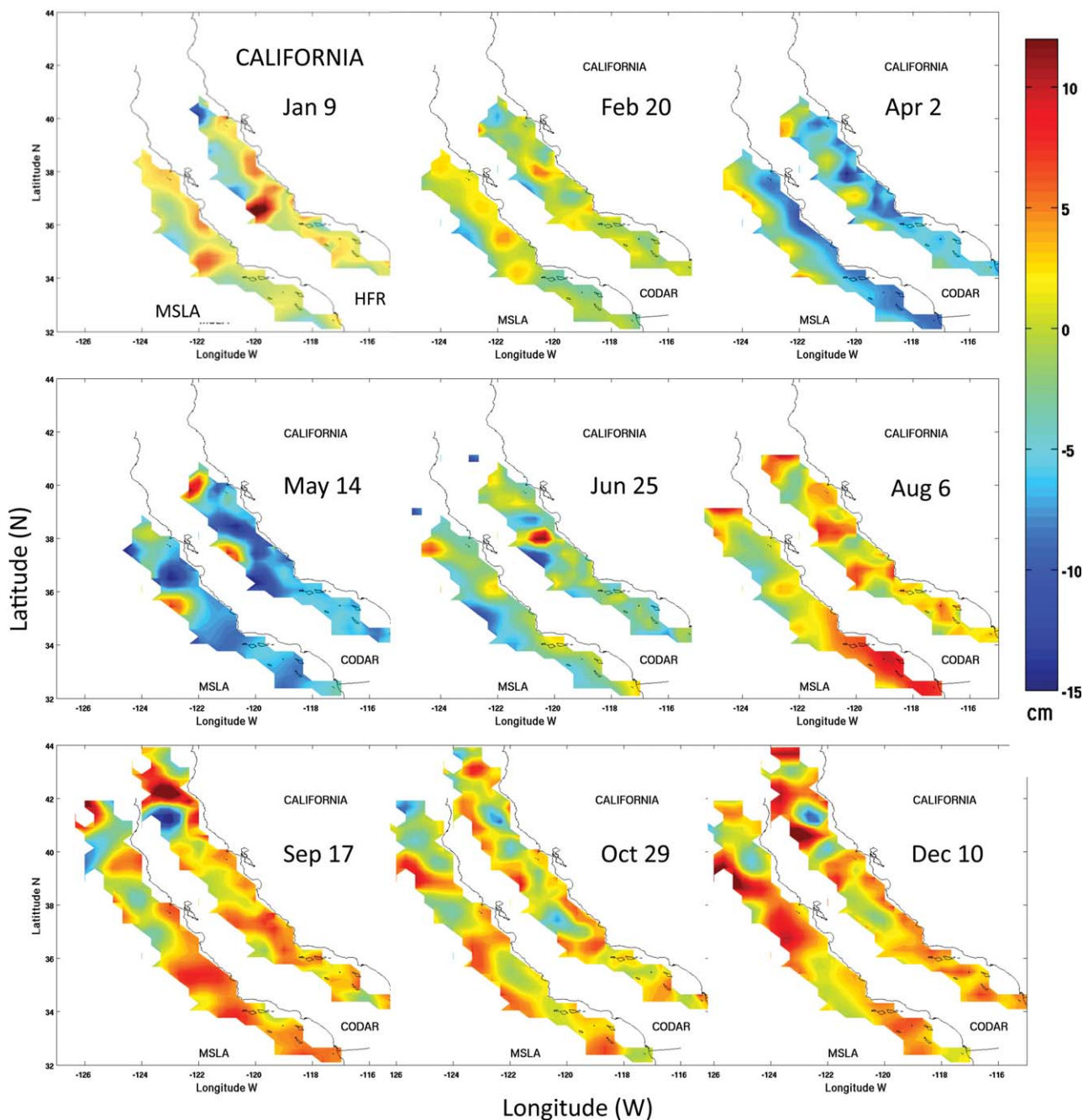
Figure 11. (bottom) Weekly AVISO MSLA compared to (top) HFR SLA every 6 weeks for 2008 along the Californian coastline, on a 1/3° × 1/3° grid. The date on the figure represents the center of the week. The SLA is given in centimeters. The HFR coverage increases after August.

extends to the north, because the coverage of the 6 km HFR grid increases. The time evolution of these two fields for the year 2008 shows excellent agreement: the formation and development of eddies is nearly identical in both series. To quantify this relationship, the SLA time series for the 51 weeks, for each grid point, in the subregion available for the whole year (as observed for the week of 9 January 2008), have been retrieved for both HFR and altimetry. The correlations for the 150 grid points between the two SLA time series (Figure 12) are excellent, except for a few grid points (25 points, 16%) where the correlations are lower than 0.7.

These points are found in the border regions, where the HFR velocities may be less reliable, as well as in the regions less sampled by the HFRs over 2008.

[61] This result, although on a large timescale and low-resolution spatial grid, suggests that the HFR-synthetic SSHs can be used as a proxy for the altimetric-measured heights in the open ocean where the waveforms are, usually, not distorted due to proximity to land.

4.1.2. HFR and Jason-1 SLA

[62] The 6 km HFR synthetic heights were computed during 2008 and interpolated along the altimeter track P221, which terminates in Monterey Bay, California
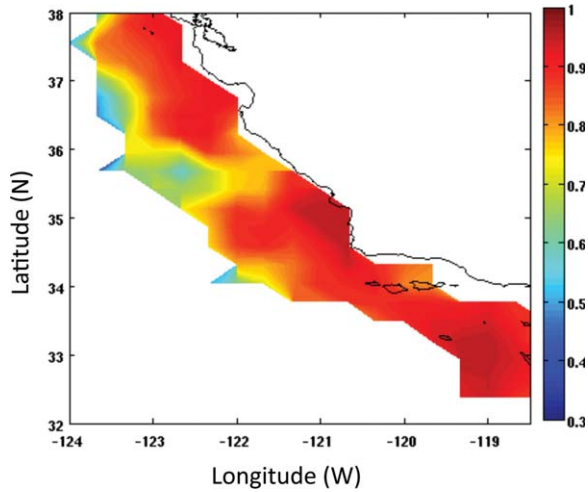
Figure 12. Mean correlation between the time series of the weekly inferred HFR and the MSLA sea levels, for each 150 grid point, on a 1/3° × 1/3° grid, over the year 2008.

(Figure 9). These were compared (first 12 cycles in Figure 13) with the coincident along-track Jason-1 standard open-ocean 1 Hz (6 km along track spacing) SLA product. The

SLA data are referenced to the same nominal ground track. To reduce the noise from the Jason-1 1 Hz set, two different filters have been applied, one with a cutoff wavelength of 50 km and the other with a cutoff wavelength of 25 km. This procedure enables us to check which level of filtering better correlates with the variability of the SLA signal retrieved from the HFR data set. The means for each time series over the 33 cycles for the year 2008 have been removed (Some Jason-1 data are missing in August).

[63] From this small sample, we can see that in about 70% of the cases both the HFR sea levels and the altimetric heights agree relatively well (first 12 cycles in Figure 13). The higher wavenumber "wiggles" in the 25 km filtered curve could depict areas where the SWH is large and the altimeter SLA is retrieved with less precision, or there are simply more detailed dynamical features in this area (for example, Figure 13, C229). In other cases, the two sets diverge in segments that seem time dependent but not related to the distance from the coast (such as Figure 13, C224 and C230). When a 25 km low-pass filter is applied to the 1 Hz altimeter SLA the correlation with the 6 km HFR sea level is low, as the former contains more noise or shorter scales ocean dynamics, and a 50 km cutoff frequency seems to smooth the data a little too much. In fact, a 40 km cutoff frequency gives only slightly different
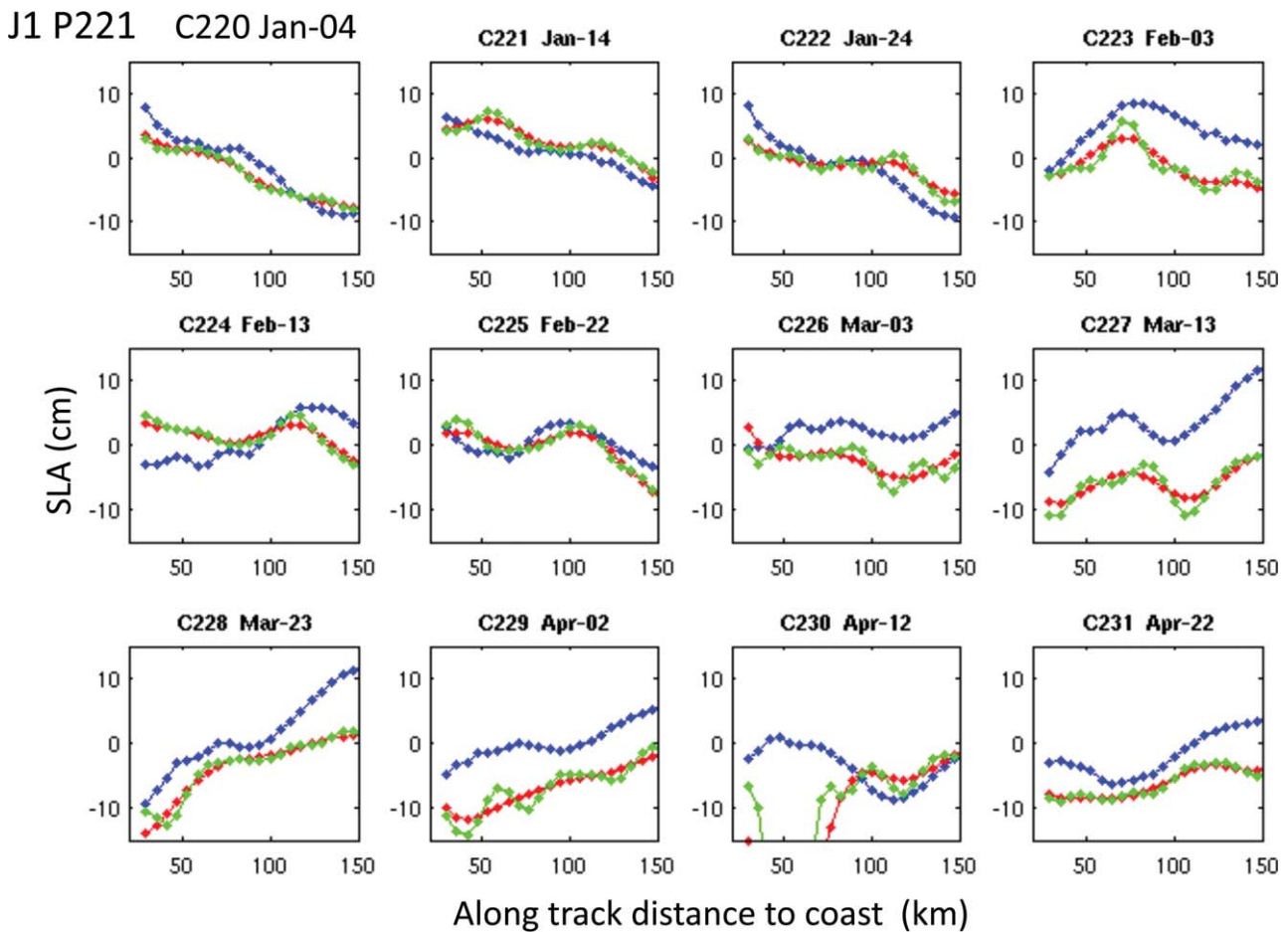
Figure 13. Comparison Jason-1 and HFR SLAs along P221 for Cycles 220 to 231. HFR SLAs (in blue) are amplified by 2 and Jason-1 1 Hz SLAs are filtered with a cutoff frequency of 50 km in red and 25 km in green.
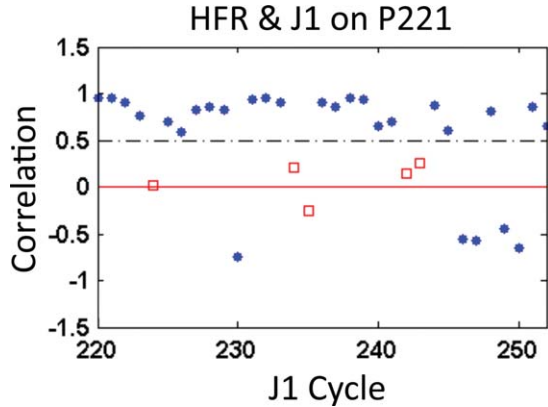
Figure 14. Correlations between the 6 km HFR inferred SLAs and the Jason-1 SLAs smoothed with a cutoff frequency of 50 km. They are computed along-track P221 on the section 50–150 km from coast, for 33 cycles in 2008. Red squares are not statistically significant.

correlations than the 50 km cutoff frequency. To quantify the relationship the correlation coefficients between the HFR heights and the 50 km filtered Jason-1 anomalies have been computed.

[64] The correlation coefficients are calculated (Figure 14) for the 33 cycles during the year 2008 and confirm our conclusions. Five sets are statistically insignificant, five sets are negatively correlated, and the remaining 23 sets have correlations larger than 0.5. The mean correlation for these 23 sets was 0.82, with the mean slope of the regression coefficient (HFR versus AVISO) around 2. This explains the consistent multiplication of the HFR-inferred SLA by a factor 2 in order to enhance the comparison.

[65] A closer inspection reveals that for cycle C230, with a correlation of -0.7, there is a problem with the altimeter data probably from a low-wind event. For cycle C226, a major portion of the sea level variations is in good agreement, but the correlation is only 0.6 because the nearshore end segment diverges. The next step is to find out if this level of matching is sufficient to detect when another retracker would be better suited.

4.2. Comparison of HFR With PISTACH Retrackers

[66] In this section, the sea levels from four retrackers are extracted from the PISTACH product. The goal is to determine if we can validate the different retrackers using the sea levels computed from the HFR currents. This comparison will be carried out with two different processing methods for the 20 Hz altimeter data: one by deriving the traditional 1 Hz data stream and the other by keeping the 20 Hz rate. The former will be compared with the sea levels derived from the 6 km HFR currents only; the latter also includes the 2 km HFR currents.

#### 4.2.1. The 1 Hz PISTACH Data Rate

[67] Each of the four PISTACH retrackers (MLE-4, Red3, Ice3, and Oce3) SLA is averaged using a 20 point boxcar window and sampled every 20 points, to create 1 Hz retracked SLAs. In this process, a simple 3 sigma filter, within the 20-point box, edits the extreme outliers. No other special editing following criteria in the GDR handbooks are done, because the goal is to evaluate the performance of the retrackers under various ocean conditions. Then, each retracked SLA series is filtered with a cutoff frequency of 25 and 50 km, and will be analyzed with the coincident 6 km HFR sea levels. For each cycle and each retracker, an unknown offset has been estimated and removed from the HFR sea levels. This offset has been calculated such that the mean of the differences between the retracked and HFR sea levels, on the track segment considered, is zero.

[68] If we assume the HFR sea levels to be the best estimate of the geostrophic field then we can evaluate the retracking techniques. At this point of study, the shapes of the SSH curves are more important than the exact values, because there may be some offset between HFR and altimetry not yet taken into account. The demeaned SLAs given by the different retrackers are displayed for six consecutive cycles C006–C0011 (Figure 15). The "x," on the figure, points to the retracker that most closely approximates the HFR set. The ovals represent segments where both curves are similar. To quantify the value of having several retrackers at our disposal, the standard deviation (STD) and the correlation coefficient time series between each retracker with the coincident HFR sea level anomalies have been computed for the 49 Jason-2 cycles from C004 to C054 (except for C005 and C018). The 1 Hz time series have 17 points on track P221 along a segment from 25 to 120 km to the coast (corresponding to the along-track distance 50–150 km, considering the geometry of the Monterey Bay coastline). Table 1 displays the individual results for the six cycles, which represents a comprehensive array of possible encountered situations.

[69] We note that Red3 and MLE-4 are very similar except for cycle C010. For cycle C008, all retrackers relate to HFR. Ice3 has the highest correlation (ρ) of 0.96. For cycle C006, the shapes differ and Ice3 performs better, but with a correlation of only 0.4. For cycle C007, only Ice3 follows the HFR profile. For cycle C009, the end segment fits with MLE-4 or Red3 and have correlations of $\sim$0.66, but the nearshore segment diverges for all retrackers. For cycle C010, the 90–150 km segment is better retracked with Ice3 or Red3, and closer to shore MLE-4 improves the match, considering the HFR as the validation set. All of the individual retrackers have a low correlation. Finally for cycle C011, all retracked SLA are similar but do not follow HFR data. For these six cycles, the STD for the best-correlated retracker is usually the lowest and is, in these cases, lower than 2 cm for correlations higher than 0.67.

[70] The Oce3 is expected to give noise-reduced and -improved SLA results. However, the outputs given in the PISTACH product are derived from an early version of the Oce3 algorithm, which contains a slight problem (P. Thibaut, personal communication, Oct. 2012). In this version, the along-track waveform series is divided into contiguous segments. For each segment, an SVD is performed and the same SVD filtering parameters are used for all the waveforms within the segment, before the MLE-3 is applied. But this methodology, as was later discovered, can create retrieved-range jumps between the segments and produce noisy-wavy like Oce3 sea levels (Oce3 C007 in Figure 15). This problem does not affect the quality of Oce3 for all cycles. When the noise level in the Oce3 (as seen in the 25 km filtered SLA) is low, the results may be trusted. For
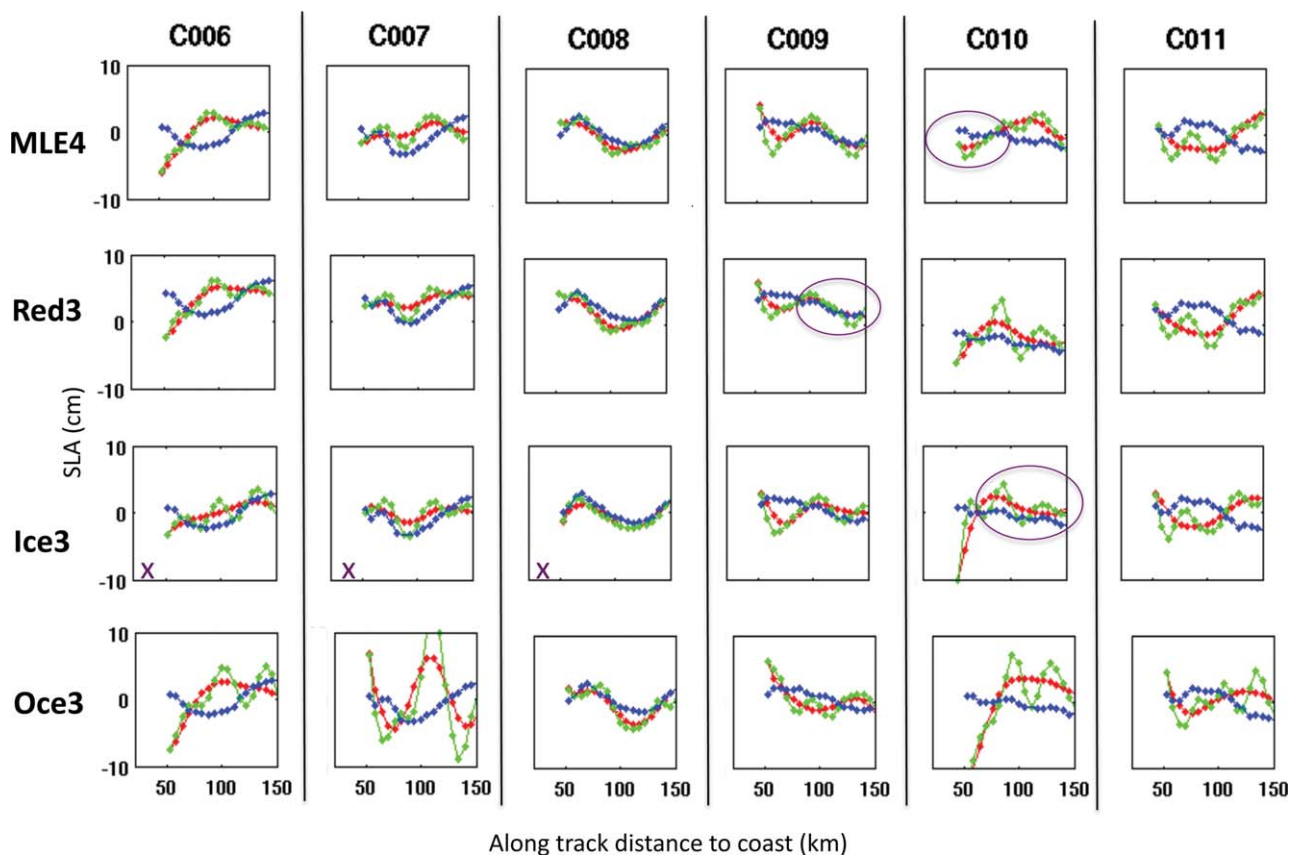
Figure 15. Comparing PISTACH retrackers with HFR sea levels, for six cycles along P221. The 1 Hz SLAs are smoothed with a cutoff frequency of 50 km in red and 25 km in green. The blue curves represent the HFR SLAs amplified by 2. The x is the retracker that best fit HFR. The ovals represent segments where both sea level shapes are similar.

example, Oce3 is consistent with the other retrackers for C008 (Figure 15). The results from Oce3 are considered in this analysis, but with precaution, knowing that its reliability is in question.

[71] In summary and clearly displayed in Figure 16, for MLE-4 and Ice3 only, there are examples when both match and either fit (Figure 16c) or do not fit (Figure 16d) HFR. There are cases when either MLE-4 (Figure 16a) or Ice3 (Figure 16b) are consistent with HFR. Finally, there are some sets where we could combine segments of MLE-4 and Ice3 in order to get closer to the, presumed more accu-

Table 1. Correlation Coefficients Between the HFR and PIS-TACH Retrackers SLAs for Six Cycles in 2008, as Well as the STD of Their Differences

	C006	C007	C008	C009	C010	C011
Correlation						
MLE-4	−0.08	0.24	0.84	0.65	−0.4	−0.9
Red3	0	0.66	0.82	**0.67**	0.03	−0.87
Ice3	**0.4**	**0.77**	**0.96**	0.07	−0.44	−0.82
Oce3	−0.08	−0.32	0.91	0.5	−0.6	−0.08
STD (cm)						
MLE-4	3.18	2.25	1.	2.1	2.34	4.25
Red3	2.9	**1.83**	1.25	**1.65**	2.36	4.37
Ice3	**2.27**	1.85	**0.88**	2.3	3.11	3.75
Oce3	4.2	6.7	1.83	2.4	5.42	3

rate, HFR SSH estimates (Figure 16e). This can be generalized to more retrackers.

[72] Next, the statistics for the 49 cycles are presented in Table 2. The mean correlation for each retracker is around 0.5. If instead, we create a retracked SLA series, where only the retracker with the highest correlation is kept, the Best-Retracker (B-RTK) sea levels, then the mean of the correlation becomes 0.68, an amelioration of about 30%. A subset of these 49 cycles is picked by keeping only the B-RTK sea level time series with a correlation larger than 0.7. There are 35 (70%) such B-RTK sets. However, for each of the four individual retrackers, the number of sets with a correlation larger than 0.7 is ~25 (50%); 10 less sets than in the combined B-RTK. The Mean of the correlation for these 35 B-RTK sets is 0.88 compared to 0.77 for the 35 corresponding MLE-4 sets, an improvement of 14%. The B-RTK contains 15 MLE-4, 11 Ice3, 4 Red3, and 5 Oce3 sets with a correlation larger than 0.7. The mean STD for these sets is 2 ± 1 cm.

[73] The regular Brown model based retrackers and Ice3 can give very similar SLA. However, Ice3 provides better results in several instances. The ice retracker, a threshold type retracker, is not based on a "physically sound" model (not derived from knowledge of microwave scattering at nadir) and care should be taken in its interpretation. This empirical model enables the retracking of waveform shapes that does not conform to the generic open ocean ones and
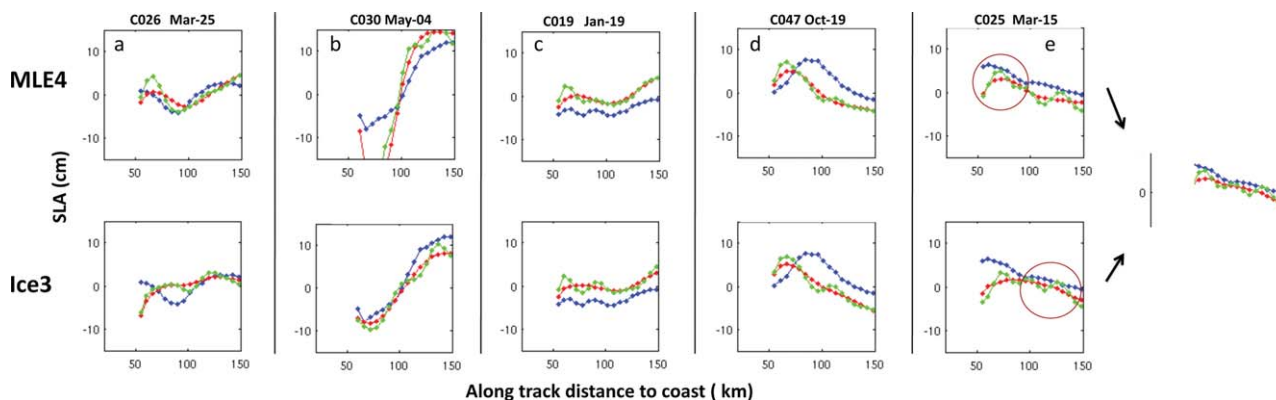
Figure 16. Comparing MLE-4 and Ice3 with HFR sea levels along P221. Same labeling as in Figure 15. (a) MLE-4 best fit; (b) Ice3 best fit; (c) All similar; (d) MLE-4 and Ice3 similar, but not to HFR; (e) Combining MLE-4 and Ice3 fits HFR.

may give better results under a wider variety of conditions. But the retrieved parameters may not have a clear connection to the underlying geophysical forces. This conclusion underlies the fact that even offshore the waveforms may diverge from the Brown model and the conventional deep ocean retrackers do not apply.

[74] If we assume that the HFR anomalies can be used as a validation tool, these statistics are in favor of the need to have various retrackers at our disposal, even over the continental shelf region. The HFR can provide the backup necessary to determine what are the associated sea surface phenomena that create the disturbances to the waveforms and contribute to less reliable estimates of the conventional open ocean retrackers.

4.2.2. The 20 Hz PISTACH Data Rate

[75] In this section, the PISTACH 20 Hz data stream will be studied employing a different processing to start examining the possibility of extracting a higher-resolution product nearshore, where the temporal and spatial variability of ocean processes increases. Instead of subsampling to the 1 Hz data rate, the original full 20 Hz rate is used. These data are noisy. To reduce the measurement noise, the 20 Hz SLA outliers are removed by using an iterative strategy that combines a low-pass filter with a 3 sigma boundary editing. Then the data is smoothed using a boxcar window of 21 points (7 km) and 60 points (21 km). Filtering the data with a cutoff frequency of 7 km will, still, create a noisy along-track sea-level series. It was kept partly to

reveal regions with more high-frequency errors that may be associated with a variable sea state or other disturbing conditions. Now we present SLA data sets that go all the way to the shore, as the level of filtering is more appropriate to deal with the end points. We can compare them with the 2 km derived HFR SSH available for the year 2009 along P221. In fact, now the nearshore 2 km HFR currents and offshore 6 km ones are combined. These observations are used to generate the 2 km OI gridded HFR sea levels that are then interpolated every 2 km (∼6 points) on the along-track P221.

[76] The 2 km HFR sea levels have more variability than the previous 6 km product (Figure 19). The question is do these reflect the structures observed in altimetry. The 21-km filtered PISTACH sea levels contain small high-frequency components that seem unrealistic (Figure 19). Their larger spatial-scale dynamics agree well with the ones of HFR, especially for the case C031 on May 14, for Ice3. For C034 on June 12, the nearshore segment 0–60 km contains small-scale features in the HFR sea levels that correspond to the variations of Ice3. If those features are realistic, then filtering altimeter data at this level can be beneficial in the nearshore regions.

4.3. Sea State

[77] Various sea state conditions can affect the quality of altimetric SSH. This can explain some of the disagreements between the HFR sea levels and those from altimetry. In this discussion, Oce3 is not considered. It is not easy to

Table 2. Correlation Coefficients and STD of the Differences Between the HFR and PISTACH Retrackers SLAs for All 49 Cycles (Top) and for a Subset of 35 Cycles Chosen Such That the Correlation for the B-RTK Is Larger Than 0.7 (Bottom)[a]

	MLE-4	Red3	Ice3	Oce3	B-RTK (Retracker With the Highest ρ)
For All 49 Cycles					
Correlation	0.48 ± 0.51	0.5 ± 0.47	0.47 ± 0.47	0.42 ± 0.51	0.68 ± 0.34
STD(cm)	3 ± 1.9	2.9 ± 1.5	2.6 ± 1.1	3.6 ± 2	2 ± 1
For 35 Cycles When ρ of B-RTK > 0.7					
Correlation	0.77 ± 0.2	0.77 ± 0.17	0.68 ± 0.36	0.67 ± 0.32	0.88 ± 0.09
STD (cm)	2.7 ± 1.9	2.7 ± 1.7	2.45 ± 1.2	3.2 ± 2	2 ± 1

[a]Each value is the mean ± STD.
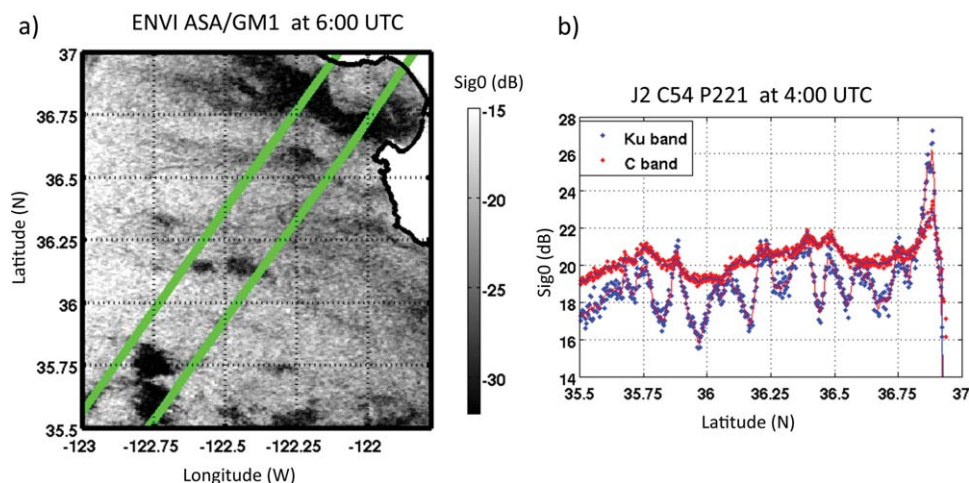
Figure 17. Backscattering coefficient sig0 for 28 December 2009 off Monterey Bay, derived from (a) Envisat ASAR at 06:00 UTC (b) Jason-2 for the Ku-band (blue), and C-band (red) at 04:00 UTC. The lines on the SAR image approximate the extent of Jason-2 P221 circular footprint.

generalize, but cases of high SWH or high Sig0 can disturb the outputs of the retrackers. For instance, the presence of unusually high-Sig0 values (Sig0 > 16 dB for Jason-2 MLE-4) in the altimeter footprint from Sig0-bloom events may signal a breakdown in the typical Brown model. The bloom events, along P221 in Monterey Bay, extend over a few tens to hundreds of kilometers. Their occurrence and frequency vary from cycle to cycle. There have been about 20% of large bloom events during the Jason-2 time series considered. As can be seen in the ENVISAT SAR image on 28 December 2009 (Figure 17) 2 h apart from the Jason-2 C054 P221 passage, small-scale variations in surface roughness over the altimeter footprint can occur. The altimeter MLE-4 retrieved Sig0 for the Ku-band and C-band are very high (> 16 dB) with wavy patterns, related to the dark patches of low-SAR backscatter. Under low wind conditions (≤ 5m/s) short gravity waves can be suppressed and a high-altimeter specular backscatter coincides with a low Bragg scattering mechanism in SAR. The knowledge of a high-resolution repartition of surface roughness over the altimeter footprint is important. During a bloom event, Ice3 behaves in a more stable manner than MLE-4 (or Red3) and stays closer to the HFR sea levels.

[78] Cycle C030, on May 4 (Figure 18), is a case when the Sig0-bloom event extends over a large region with Sig0 > 20 dB; none of the filtered 20 Hz retrackers are well adapted in this situation. The HFR sea levels, available throughout, have large variations (−15 to +15 cm). Can they be used to correct altimetry during this bloom event? We mentioned, in section 2.2, that there can be a lack of HFR data in case of low wind events, but these have been observed to last less than a few hours over 2009. By doing a 3 day average, we can still get an estimate of the SSHs. In this case, for C030, the answer is probably yes, because, interestingly, at the 1 Hz data rate Ice3 corrected this bloom event very well (Figure 16).

[79] Note that we chose to use the MLE-4 derived Sig0, as an indication of the sea state or problematic zone, from a well-studied, traditional open ocean retracker. Historically, MLE-4 was implemented to correct for the Jason-1 attitude

problem, and estimates the slope of the trailing edge related to the mispointing angle. It was then chosen to retrack Jason-2 echoes. MLE-4 gives better estimates of range and SWH, relative to MLE-3, but Sig0 is degraded because the joint estimation of the mispointing and Sig0 is ill conditioned [*Thibaut et al.*, 2010]. As a reminder, the new GDR version "D" includes both the MLE-3 and MLE-4 outputs and their Sig0 have different characteristics. For example,
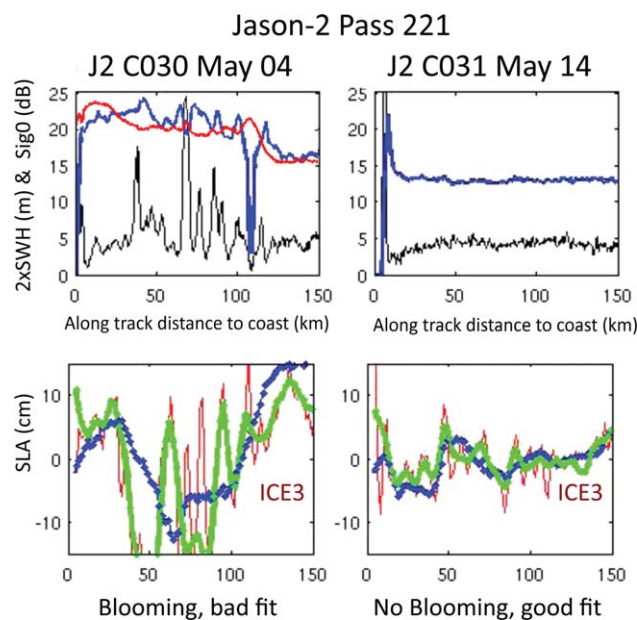
Figure 18. Comparison HFR and Ice3 SLAs along P221, (left) with and (right) without bloom. (top) Sig0 (dB) from MLE-4 in blue, SWH (m) amplified by 2 in black. Bloom events occur for Sig0 > 16 dB for Jason-2. Close to shore there is contamination by land. For Sig0 ∼ 0 dB, there is a loss of signal by the tracker. Sig0 from Red3 is displayed in red for C030. (bottom) HFR SLAs are amplified by 2, in blue; Jason-2 20-Hz Ice3 SLAs are filtered with a cutoff frequency of 7 km in red and 21 km in green.
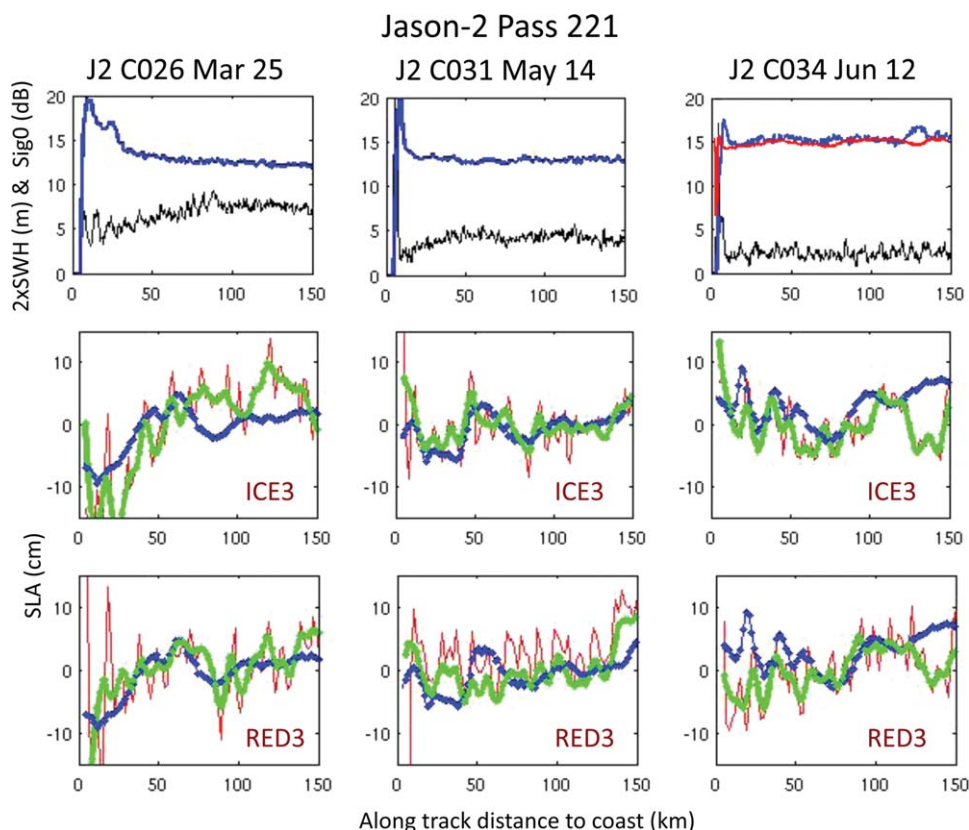
Figure 19. Comparing (middle) Jason-2 ICE3 and (bottom) RED3 retrackers with HFR SLAs for different sea states along P221 (same color code as in Figure 18). Sig0 from Red3 is displayed for C034 in red.

Figure 18 shows the Sig0 profiles for MLE-4 and Red3 (which is based on MLE-3) during a bloom event. The MLE-4 derived Sig0 contains more noise level and one can observe more undulations. The Red3 and MLE-4 derived SWH exhibit very similar behavior in the cases presented, so only the MLE-4 SWH is displayed.

[80] We examined three cases, along P221, to compare the response of the Ice3 and Red3 retrackers depending on the sea state as described by the altimeter MLE-4 derived SWH and Sig0 (Figure 19):

[81] (1) Cycle C031: There are no bloom events, Sig0 stays below 15 dB, and SWH below 2.5 m. Ice3 performs well and better than Red3 throughout.

[82] (2) Cycle C026: Beyond the close to shore bloom events (<30 km) Red3 performs better though it seems noisy. In this case, the SWH is relatively high, starting at 2.5 m and increasing to 5 m offshore.

[83] (3) Cycle C034: Low SHW < 1.5 m. Ice3 matches well closer than 50 km, then Red3 until a little bloom event around 140 km. For this example, the Red3 Sig0 is displayed, because it has an opposite behavior in the region of the bloom event as seen by MLE-4. Any difference may signal a breakdown of the assumed Brown model waveforms.

[84] To summarize, using only Ice3 and MLE-4, for Sig0-bloom events, Ice3 is more stable. When both SWH is low and Sig0 is less than 16 dB, the sea levels from MLE-4 and Ice3 are very similar (Figure 10, C019). When the

SWH is high (SWH > 3 m, associated with low Sig0, high wind speeds) or SWH is variable within the segment, Ice3 and MLE-4 can differ. It these instances MLE-4 seems to better fit the HRF sea levels (Figure 10, C016). Although we generalized, along a track the best fit relative to HFR sea levels can change in an unpredictable fashion, it is not clear under which conditions one retracker would be more efficient than the other. This needs to be investigated more systematically to see if we could predict a trend.

[85] As mentioned in the last section, there are cases when only one segment of a retracker fits the HFR sea levels and cases when the HFR and altimeter sea level sets diverge. Besides the bloom events, there are about 15 cases when both data sets are not quite similar, either as a phase shift or as an end segment. One of the future tasks will be to determine which one is a better representation of the true sea surface level. There are limitations inherent to the HFR measurements and OI processing that need to be better evaluated to define how effectively we could use the HFR sea levels as a reference to improve the quality of altimetry.

5. Discussion and Conclusion

[86] One of the challenges of using satellite altimetry in the coastal ocean is correcting for distortions of the altimetric waveforms linked to the presence of possible rapid changes in sea states and/or the presence of land within the

altimeter footprint. Many retracking procedures have been developed, but there is great difficulty in knowing what is the proper method and where it is best applied. We evaluated the skills of the HFR coastal surface currents to validate the retrackers, especially in the region 25–150 km offshore. The U.S. West Coast HFR network monitors hourly ocean surface currents with an offshore range up to 150 km and spatial resolutions of 2 and 6 km depending on the radar operating frequency. By analyzing the time- and space scales of the coastal oceanic features, we can fit a stream function to the HFR coastal currents to retrieve their matching SSHs, which are mapped with varying spatial scales using OI. Tested on regions more than 25 km off the California coast, we demonstrate a similarity between the HF coastal radar derived SSH fields and those computed directly from standard satellite altimetry product using Jason-1 and Jason-2 over the years 2008 and 2009.

[87] The behavior of four retrackers from Jason-2 PISTACH coastal product were analyzed and showed the possibility of determining which retracker better fits the HFR sea levels depending on the sea state and other conditions. The PISTACH version of Oce3 is not reliable. Red3 and MLE-4 give very similar results, for the sea level, over the offshore regions. This is not surprising as both retrackers are based on the MLE fits using the Brown model. Red3 uses observations only centered on the leading edge instead of the complete waveform. Red3 will provide better estimates of the sea level when the trail end part is distorted. The largest differences are seen between MLE-4 and Ice3. Ice3 is more stable when the waveforms depart from the standard open ocean shape, for example, during Sig0-bloom events. But Ice3 is not based on a physical model, so care must be taken in its interpretation.

[88] Having the HFR sea levels to validate the retrackers demonstrated a tendency to have Ice3 fit better in cases of bloom events and MLE-4 (or Red3) in cases of high SWH. There are cycles when the match is almost perfect. There are also instances when the HFR and altimetry do not agree, either on segments or for the complete track considered. If we keep a time series of best fitted retracker (B-RTK), relative to HFR, then the mean correlation, at the 1 Hz level, is higher than 0.7, seventy percent of the time along-track P221 on the portion 25 km to 120 km offshore. The mean correlation for this 70% subset is 0.88. This result is without combining several retrackers on an individual track.

[89] A different processing strategy was implemented on the altimeter data, to use the original full 20 Hz rate, instead of subsampling to 1 Hz. The 20 Hz SLA outliers are edited with an iterative strategy that combines a low-pass filter with a 3 sigma boundary editing. Then the data is smoothed with a 21 km boxcar window. At this level of filtering, the SLAs are still contaminated by high-frequency signals. But we find that it contains additional information about oceanic processes, in the coastal zone, by referencing them to the 2 km resolution HFR sea levels.

[90] The processing of both data sets still requires improvements to make them more compatible and understand the limitations of this comparison. For instance there are some issues with the HFR surface currents inversion methodology. Three-day-averaged HFR currents are used as input to the OI, but perhaps a 1 day average would be
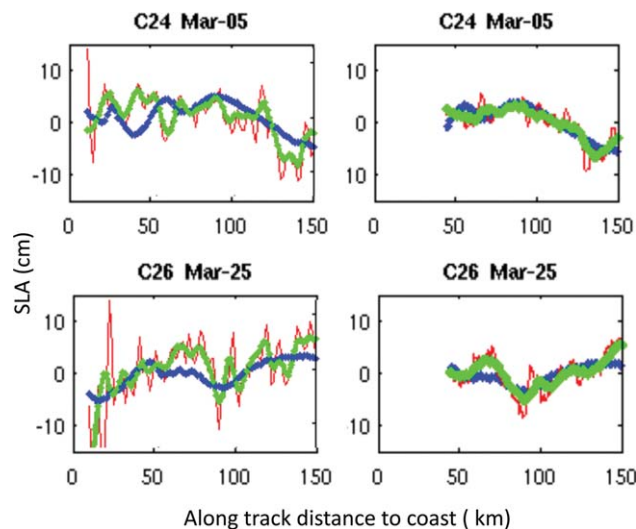
Figure 20. (left) No editing and (right) edited MLE-4 with HFR sea levels (in blue). The MLE-4 sea levels are both filtered with a cutoff frequency of 7 km in red and 21 km in green. But on the right, spurious data are removed, before filtering, and refines the 20 Hz MLE-4 SLAs.

more representative of the instantaneous altimeter along-track SSH. How stringent should the quality of the HFR currents be, which would lead to data gaps in the HR coverage? Finally there is the issue of a variable HFR synthetic heights multiplicative factor around 2, in order to bring them to the same signal level as those from altimetry. What is its origin, and how should it be accounted for in the inversion process? Perhaps, a comparison between HFR currents and altimetric geostrophic currents can help us resolve this problem.

[91] For the altimeter processing, the concerns are about editing (depending on the goals) and finding the best filtering to match the HFR heights variations. For example, spurious data, known to be less reliable offshore (Sig0 > 16 dB and/or SWH > 5 m), are edited from the 20 Hz MLE-4 data before filtering with a 21 km boxcar window. This results in a noise-reduced altimeter SLA (Figure 20). This strategy can be used to compare HFR sea levels with altimetry in situations when, only, reliable altimeter measurements are required.

[92] There are limitations inherent to the HFR data that need to be better evaluated to define how effectively it can detect the erroneous altimetric data and be used as a reference to improve their quality. Some dissimilarity, between the HFR/altimetric SSH comparisons, arises because the principal measurements of both instruments capture different physical phenomena. To address the last point, a reliable and quantifiable correspondence between the altimetric SSH and the independent inferred SSH should be established. This can be done first in the offshore regions, in situations when the standard-retracked altimeter data are reliable. This means that, in a first step, the altimeter data will give feedback on the validity of the technique, as well as how to improve the HFR sea levels. In a second step, the cases when the two sets diverge will be analyzed and checked to determine which one is a better estimate of the true sea surface parameter; by looking at the waveforms, or

by introducing auxiliary information (sea surface temperature, ocean color). The influence of the seasonal currents or wind patterns can also be examined on the quality of the HFR sea levels. Then the analysis can be extended toward the coastline.

[93] Overall, these preliminary studies have demonstrated the value of HFR surface currents as a promising tool to validate and find new strategies to correct coastal altimetric SSHs. They also provide some insight into the altimeter behavior as a function of ocean conditions to account for some oceanic mechanisms and various sea states, particular to the continental shelf, that affect the conventional altimeter measurements. The optimal method for altimetry retracking seems to be a combination of different retrackers for various segments of the altimeter track and depends on the cycle. The experience gained from a systematic comparison of both data sets can provide hints on how to correct conventional coastal altimetry when no HFR arrays are deployed. Maybe we can find a relationship between the behavior of the waveform series around the point of concern and the quality of the fit HFR with altimetry SSH; or possibly a relationship between the Ku-band derived Sig0 and the C-band derived Sig0 can help detect when the conventional ocean retracker is not optimal and refine the choice of retracker. These clues will apply to the immediate oceanic area.

[94] The implementation of the methodology to other coastal regions will depend on the specifics of the regional coastal zone dynamics. The parameters between HFR and altimetry SSH may need some adjustments, not only in the spatial scales used in the OI but also in the linear correspondence between the two sets. For instance the continental shelf in the North Atlantic Bight, along the U.S. east coast, is very wide and shallow relative to the one on the U.S. West Coast. This study is a guide on what should be done in other areas.

[95] There are cases when the match between altimetric and HFR along-track sea levels is almost perfect and cannot be coincidence only. Once the conditions for a consistency between the HFR and altimeter data are established, the HFR surface currents would be invaluable for the validation of future altimetry missions, better suited for coastal regions, when those conditions are met.

References

Andersen, O. B., and R. Scharroo (2011), *Range and Geophysical corrections in coastal regions and implications for mean sea surface determi-*

nation, in Coastal Altimetry, edited by S. Vignudelli et al., pp.103–145, Springer, Berlin, doi:10.1007/978-3-642-12796-0.

AVISO/Altimetry (2010), Coastal and Hydrology Altimetry Product (PISTACH) Handbook, CLS-DOS-NT-10–246, SALP-MU-P-OP-16031-CN 01/00, ed.1.0, CNES/CLS, France, http://www.aviso.oceanobs.com/file admin/documents/data/tools/hdbk_Pistach.pdf.

AVISO/Altimetry (2012), SSALTO/DUACS Users Handbook DT CorSSH and DT SLA Product, CLS-DOS-NT-086.381, ed. 2.0. CNES/CLS, France, http://www.aviso.oceanobs.com/fileadmin/documents/data/tools/hdbk_dt_corssh_dt_sla.pdf.

AVISO/Altimetry (2013), SSALTO/DUACS Users Handbook MSLA and MADT Near-Real Time and Delayed Time Products, CLS-DOS-NT-06.034, SALP-MU-P-EA-21065-CLS, ed.3.4, CNES/CLS, France, http://www.aviso.oceanobs.com/fileadmin/documents/data/tools/hdbk_duacs.pdf.

Barrick, D. E., M. W. Evans, and B. L. Weber (1977), Ocean surface currents mapped by radar, *Science*, *198*, 138–144, doi:10.1126/science.198.4313.138.

Birol, F., M. Cancet, and C. Estournel (2010), Aspects of the seasonal variability of the northern current (NW Mediterranean Sea) observed by altimetry, *J. Mar. Syst.*, *81*, pp. 297–311, doi:10.1016/j.jmarsys.2010.01.005.

Bouffard, J., S. Vignudelli, M. Hermann, F. Lyard, Marsaleix, Y. Ménard, and P. Cipollini (2008), Comparison of ocean dynamics with a regional circulation model and improved altimetry in the North-western Mediterranean, *Terr. Atmos. Ocean. Sci.*, *19*, 117–133, doi:10.3319/TA0.2008.19.1–2117(SA)

Bretherton, F. D., R. E. Davis, and C. B. Fandry (1976), A technique for objective analysis and design of oceanographic experiments applied to MODE-73, *Deep Sea Res.*, *23*, 559–582.

Brown, G. (1977), The average impulse response of a rough surface and its applications, *IEEE Trans. Antennas Propag.*, *25*, 67–74.

Brown, S. (2010), A novel near-land radiometer wet path-delay retrieval algorithm: Application to the Jason-2/OSTM advanced microwave radiometer, *IEEE Trans. Geosci. Remote Sens.*, *48*(4), 1986–1992, doi:10.1109/TGRS.2009.2037220.

Chavanne, C. P., and P. Klein (2010), Can oceanic submesoscale processes be observed with satellite altimetry?, *Geophys. Res. Lett.*, *37*, L22602, doi:10.1029/2010GL045057.

Chelton, D., J. Ries, B. Haines, L. Fu, and P. Callahan (2001), *Satellite altimetry, in Satellite Altimetry and Earth Sciences: A Handbook of Techniques and Applications*, edited by L. Fu and A. Cazenave, pp. 1–132, Elsevier, New York.

Chereskin, T. K., and M. Trunnell (1996), Correlation scales, objective mapping, and absolute geostrophic flow in the California Current, *J. Geophys. Res.*, *101*, 22,619–22,629, doi:10.1029/96JC02004.

Cipollini, P., S. Vignudelli, F. Lyard, and L. Roblou (2008), *15 years of altimetry at various scales over the Mediterranean, in Remote Sensing of European Seas*, edited by V. Barale and M. Gade, pp. 296–306, Springer, Heidelberg, Germany, doi:10.1007/978-1-4020–6772-3–22.

Davis, C. H. (1997), A robust threshold retracking algorithm for measuring ice-sheet surface elevation change from satellite radar altimetry, *IEEE Trans. Geosci. Remote Sens.*, *35*(4), 974–979.

Deng, X. (2004), Improvement of geodetic parameter estimation in coastal regions from satellite radar altimetry, Ph.D. thesis, 248 pp., Curtin Univ. of Technol., Perth, Australia.

Deng, X., and W. E. Featherstone (2006), A coastal retracking system for satellite radar altimeter waveforms: Application to ERS-2 around Australia, *J. Geophys. Res.*, *111*, C06012, doi:10.1029/2005JC003039.

Deng, X., W. E. Featherstone, C. Hwang, and P. A. M. Berry (2002), Estimation of contaminations of ERS-2 and POSEIDON satellite radar altimetry close to the coasts of Australia, *Mar. Geod.*, *25*(4), 249–271.

Deng, X., W. E. Featherstone, C. Hwang, and C. Shum (2003), *Improved coastal marine gravity anomalies at the Taiwan Strait from altimeter waveform retracking*, in International Association of Geodesy Symposia, vol. 126, edited by C. Hwang, C. Shum, and J. Li, pp. 41–45, Springer, Berlin, Heidelberg.

Desporte, C., E. Obligis, and L. Eymard (2007), On the wet tropospheric correction for altimetry in coastal regions, *IEEE Trans. Geosci. Remote Sens.*, *45*(7), 2139–2149, doi:10.1109/TGRS.2006.888967.

Gómez-Enri, J., I. Caballero, G. Navarro, and P. Villares (2011), Towards a validation of ENVISAT RA-2 high rate significant wave height in coastal systems: Case study of the Gulf of Cadiz, paper presented at 5th EARSeL Workshop on Remote Sensing of the Coastal Zone, Prague, Czech Republic, June 2011.

Gommenginger, C., P. Thibaut, L. Fenoglio-Marc, X. Deng, J. Gómez-Enri, and Y. Gao (2011), *Retracking altimeter waveforms near the coasts, in Coastal Altimetry*, edited by S. Vignudelli et al., pp.61–10, Berlin, Springer, doi:10.1007/978-3-642-12796-0.

Herbert, G., N. Ayoub, P. Marsaleix, and F. Lyard (2011), Signature of the coastal circulation variability in altimetric data in the Southern Bay of Biscay during winter and fall 2004, *J. Mar. Sys.*, v88, 2, 139–158, doi:10.1016/j.jmarsys.2011.03.004.

Hickey, B. M. (1998), Coastal oceanography of Western North America from the tip of Baja California to Vancouver Island, *The Sea*, *11*, 345–393.

Hwang, C., and S. A. Chen (2000), Circulation eddies over the South China Sea derived from Topex/Poseidon altimetry, *J. Geophys. Res.*, *105*, 23,943–23,965.

Hwang, C., J. Guo, X. Deng, H. Y. Hsu, and Y. Liu (2006), Coastal gravity anomaly from retracked Geosat/GM altimetry: Improvement, limitation and role of airborne gravity data, *J. Geod.*, 80, 204–216, doi:10.1007/s00190-006-0052-x.

Ikeda, M., W. J. Emery, and L. A. Mysak (1984), Seasonal variability in meanders of the California current system off Vancouver Island, *J. Geophys. Res.*, *89*, 3487–3505, doi:10.1029/JC089iC03p03487.

Kim, S. Y. (2010), Observations of submesoscale eddies using high-frequency radar-derived kinematic and dynamic quantities, *Cont. Shelf Res.*, *30*, 1639–1655, doi:10.1016/j.csr.2010.06.011.

Kim, S. Y., E. J. Terrill, and B. D. Cornuelle (2008), Mapping surface currents from HF radar radial velocity measurements using optimal interpolation, *J. Geophys. Res.*, *113*, C10023, doi:10.1029/2007JC004244.

Kim, S. Y., et al. (2011), Mapping the U.S. West Coast surface circulation: A multiyear analysis of high-frequency radar observations, *J. Geophys. Res.*, *116*, C03011, doi:10.1029/2010JC006669.

Laws, K. E., and J. D. Paduan (2011), Error assessment of HF radar based ocean current measurements: An error model based on sub-period measurement variance, paper presented at IEEE/OES Current, Waves and Turbulence Measurement Conference, *Monterey, Calif.*

Lebedev, N. A., A. G. Kostianoy, A. I. Ginzburg, D. P. Medvenev, N. A. Sheremet, and S. N. Shauro (2011), *Satellite altimetry applications in the Barents and White Sea, in Coastal Altimetry*, edited by S. Vignudelli et al., pp. 389–415, Springer, Berlin doi:10.1007/978-3-642-12796-0.

Lee, H., C. Shum, Y. Yi, M. Ibaraki, J. Kim, A. Braun, C. Kuo, and Z. Lu (2009), Louisiana wetland and water level monitoring using retracked TOPEX/POSEIDON altimetry, *Mar. Geod.*, *32*, 284–284, doi:10.1080/0149041090394767.

Lee H., C. Shum, W. Emery, X. Deng, C. Roesler, Y. Yi, C. Kuo, Z. Lu, and S. Calmant (2010), Validation of Jason-2 altimeter data by waveform retracking over California coastal ocean, *Mar. Geod.*, *33*(1), 304–316, doi:10.1080/01490419.2010.488982.

Le Hénaff, M., L. Roblou, and J. Bouffard (2010), Characterizing the Navidad current interannual variability using coastal altimetry, *Ocean Dyn.*, *61*, 425–437, doi:10.1007/s10236-010-0360-9.

Lipa, B. J., and D. E. Barrick (1986), Extraction of sea state from HF radar sea echo: Mathematical theory and modeling, *Radio Sci.*, *21*(1), 81–100, doi:10.1029/RS021i001p00081.

Liu Y., R.H. Weisberg, S. Vignudelli, L. Roblou and C.R.Merz (2012), Comparison of the X-TRACK altimetry estimated currents with moored ADCP and HF radar observations on the West Florida Shelf, *Adv. Space Res.*, *50*(8), 1085–1098, doi:10.1016/j.asr.2011.09.012.

Lyard, F., F. Lefèvre, T. Letellier, and O. Francis (2006), Modelling the global ocean tides: Modern insights from FES2004, *Ocean Dyn.*, *56*(5–6), 394–415, doi:10.10007/s10236-006-0086-x.

Mitchum, G., D. Hancock, G. Hayne, and D. Vandemark (2004), Blooms of Sig0 in the Topex radar altimeter data, *J. Atmos. Oceanic Technol.*, *21*, 1232–1245, doi:10.1175/1520–04226(2004)021.

Morrow, R., and P. Y. Le Traon (2006), *15 years of satellite altimetry and Mesoscale Ocean Dynamics observed with 15 years of altimetric data, paper presented at the Symposium on 15 Years of Progress in Radar Altimetry*, Venice, Italy, ESA.

Ohlmann C., P. White, L. Washburn, B. Emery, E. Terrill, and M. Otero (2007), Interpretation of coastal HF radar-derived surface currents with high-resolution drifter data, *J. Atmos. Oceanic Technol.*, *24*, 666–680, doi:10.1175/JTECH1998.1.

OSTM/Jason-2 Products Handbook (2011), SALP_MU_M_OP_15815_CN, ed1.8, CNES, France, http://www.aviso.oceanobs.com/fileadmin/documents/data/tools/hdbk_j2.pdf.

Paduan, J. D., and H. C. Graber (1997), Introduction to high-frequency radar: Reality and myth, *Oceanography*, *10*, 36–39.

Paduan, J. D., K. C. Kim, M. S. Coock, and F. P. Chavez (2006), Calibration and validation of direction-finding high-frequency radar ocean surface current observations, *IEEE J. Oceanic Eng., 31*(4), 862–875, doi:10.1109/JOE.2006.886195.

Quartly, G. D., M. A. Srokosz, and T. H. Guymer (1998), Understanding the effects of rain on radar altimeter waveforms, *Adv. Space Res.*, *22*(11), 1567–1570.

Ruiz S., A. Pascual, B. Garau, I. Pujol, and J. Tintoré (2009), Vertical motion in the upper ocean from glider and altimetry data, *Geophys. Res. Lett.*, *26*, L14607, doi:10.1029/2009GL038569.

Saraceno M., P. T. Strub, and P. M. Korso (2008), Estimates of sea surface height and near-surface alongshore coastal currents from combinations of altimeters and tide gauges, *J. Geophys. Res.*, *113*, C11013, doi:10.1029/2008JC004756.

Severini, J. (2010), Estimation et classification de Signaux Altimétriques, Ph.D. thesis, p.160, IPN, Toulouse, France.

Strub, P. T., Kosro, P. M., and A. Huyer (1991), The nature of the cold filaments in the California Current System, *J. Geophys. Res.*, *96*, 14,743–14,768.

Thibaut, P., J. C. Poisson, E. Bronner, and N. Picot (2010), Relative performance of the MLE3 and MLE4 retracking algorithms on Jason-2 altimeter waveforms, *Mar. Geod.*, *33*, 1, 317–335, doi:10.1080/01490419.2010.491033.

Tisch, T. D., S. R. Ramp, and C. A. Collins (1992), Observations of the geostrophic current and water mass characteristics off Point Sur, California, from May 1988 through November 1989, *J. Geophys. Res.*, *92*, 12,535–12,555, doi:10.1029/92JC01094.

Tournadre, J., B. Chapron, N. Reul, and D. C. Vandemark (2006), A satellite altimeter model for ocean slick detection, *J. Geophys. Res.*, *111*, C04004, doi:10.1029/2005JC03109.

Tran, N., S. Labroue, S. Phillips, E. Bronner, and N. Picot (2010), Overview and update of the sea state bias corrections for the Jason-2, Jason-1 and TOPEX missions, *Mar. Geod.*, *33*(S1), 348–362, doi:10.1080/01490419.2010.487788.

Walstadt, L. J., J. S. Allen, P. M. Korso, and A. Huyer (1991), Dynamics of the coastal transition zone through data assimilation studies, *J Geophys Res*, *96*, 14,956–14,977.

Wilkin, J. L., M. S. Bowen, and W. J. Emery (2002), Mapping mesoscale currents by optimal interpolation of satellite radiometer and altimeter data, *Ocean Dyn.*, *52*(3), 95–103, doi:10.1007/s10236-001-0011-2.